

RESEARCH ARTICLE

10.1002/2016JB013901

Key Points:

- Seismic anisotropy observations from the lowermost mantle beneath Australia
- Forward modeling with elastic tensors of lowermost mantle minerals
- Constrain possible dominant slip systems and orientations of mantle deformation for postperovskite using anisotropy observations

Supporting Information:

- Supporting Information S1
- Table S1
- Table S2
- Table S3

Correspondence to:

N. Creasy,
neala.creasy@yale.edu

Citation:

Creasy, N., M. D. Long, and H. A. Ford (2017), Deformation in the lowermost mantle beneath Australia from observations and models of seismic anisotropy, *J. Geophys. Res. Solid Earth*, 122, doi:10.1002/2016JB013901.

Received 24 DEC 2016

Accepted 14 JUN 2017

Accepted article online 16 JUN 2017

Deformation in the lowermost mantle beneath Australia from observations and models of seismic anisotropy

Neala Creasy¹ , Maureen D. Long¹ , and Heather A. Ford² 

¹Department of Geology and Geophysics, Yale University, New Haven, Connecticut, USA, ²Department of Earth Sciences, University of California, Riverside, California, USA

Abstract Observations of seismic anisotropy near the core-mantle boundary may yield constraints on patterns of lowermost mantle flow. We examine seismic anisotropy in the lowermost mantle beneath Australia, bounded by the African and Pacific Large Low Shear Velocity Provinces. We combined measurements of differential splitting of *SKS-SKKS* and *S-ScS* phases sampling our study region over a range of azimuths, using data from 10 long-running seismic stations. Observations reveal complex and laterally heterogeneous anisotropy in the lowermost mantle. We identified two subregions for which we have robust measurements of *D*"-associated splitting for a range of ray propagation directions and applied a forward modeling strategy to understand which anisotropic scenarios are consistent with the observations. We tested a variety of elastic tensors and orientations, including single-crystal elasticity of lowermost mantle minerals (bridgmanite, postperovskite, and ferropericlase), tensors based on texture modeling in postperovskite aggregates, elasticity predicted from deformation experiments on polycrystalline MgO aggregates, and tensors that approximate the shape preferred orientation of partial melt. We find that postperovskite scenarios are more consistently able to reproduce the observations. Beneath New Zealand, the observations suggest a nearly horizontal [100] axis orientation with an azimuth that agrees well with the horizontal flow direction predicted by previous mantle flow models. Our modeling results further suggest that dominant slip on the (010) plane in postperovskite aggregates provides a good fit to the data but the solution is nonunique. Our results have implications for the mechanisms of deformation and anisotropy in the lowermost mantle and for the patterns of mantle flow.

1. Introduction

Plate tectonics are the surface expression of mantle flow; however, the pattern of flow in the mantle can be difficult to constrain. In the upper mantle, inferences on flow can come from seismic anisotropy observations, but for the deep mantle we typically rely on modeling approaches. There are many assumptions and limitations in the construction and validation of global mantle flow models including computational cost [e.g., *Stadler et al.*, 2010]. Introducing realistic 3-D complexity from Earth's properties into these models is a challenge, in part because we have few observations that can constrain flow (and thus inform modeling approaches) in the deep mantle [*Nowacki et al.*, 2011]. Seismic anisotropy is one observable that has the potential to shed light on the geometry of deformation and thus the pattern of flow at the base of the mantle. In contrast to the bulk of the lower mantle, which is apparently isotropic [*Meade et al.*, 1995], there are many observations of anisotropy in the *D*" layer at the base of the mantle using similar techniques to this study [*Wookey et al.*, 2005a; *Wang and Wen*, 2007].

Relating seismic anisotropy observations to potential deformation scenarios in the deep mantle is no easy task, as the mechanism that produces anisotropy in the lowermost mantle remains poorly understood [e.g., *Garnero and McNamara*, 2008; *Nowacki et al.*, 2011]. All of the major minerals that may be present in the lowermost mantle (bridgmanite, ferropericlase, and postperovskite) are expected to have significant single-crystal anisotropy [e.g., *Karki et al.*, 1999; *Wookey et al.*, 2005a; *Stackhouse et al.*, 2005]; however, an aligned texture is necessary to produce an observable anisotropy signal over seismic wavelengths [e.g., *Nowacki et al.*, 2011]. The formation of lattice or crystal preferred orientation (LPO) requires deformation in the dislocation creep regime [e.g., *Karato*, 2012]. Some studies have shown that deformation to high strains in the dislocation creep regime may be possible in the lowermost mantle [e.g., *McNamara et al.*, 2001; *Nowacki et al.*, 2011], while much of the lower mantle may deform via diffusion creep [*Meade et al.*, 1995]. Alternatively, the shape-preferred orientation (SPO) of isotropic but

elastically distinct material, such as partial melt aligned via deformation, can give rise to anisotropy [e.g., Kendall and Silver, 1998]. Distinguishing between these possibilities can be difficult, as many observational studies of seismic anisotropy in D'' assume a simplified geometry, such as vertical transverse isotropy [e.g., Nowacki *et al.*, 2011].

Further complicating the issue, it is not well known which mineral phase(s) might be contributing to anisotropy for LPO scenarios. Additionally, the single-crystal elasticity of these materials at the relevant pressures and temperatures, typically studied through *ab initio* calculations, is imperfectly known [e.g., Wookey *et al.*, 2005b; Stackhouse *et al.*, 2005; Karki *et al.*, 1999]. Most crucially, the dominant slip systems—and thus the likely patterns of texture development—are not yet completely known for realistic lowermost mantle conditions, in part because of the difficulty of performing experiments at high pressure and temperature (as summarized in Nowacki *et al.* [2011], and references therein). From an observational point of view, the fact that many body wave studies of lowermost mantle anisotropy are limited to a single set of raypaths with similar geometry means that seismic data cannot typically distinguish among different possible models for anisotropy.

Despite the challenges, understanding the mechanism and geometry of seismic anisotropy is crucial to understanding the pattern of flow at the base of the mantle. The interpretation of seismic anisotropy in D'' may eventually help to constrain the mantle's composition and rheology, the generation of mantle plumes, the fate of paleo-subducted slabs, and the origins of hot spot volcanism, since these features play a key role in mantle convection (as summarized in Hernlund and McNamara [2015]). Specifically, an understanding of the (present-day) pattern of flow at the base of the mantle, as inferred from seismic anisotropy observations, would shed light on the driving forces for lowermost mantle flow and the dynamic interactions of various lower mantle structures. Additionally, constraints on the mechanism of D'' anisotropy, particularly which mineral phases contribute, may eventually help to constrain lowermost mantle mineralogy. It has been suggested that hot spot volcanism at the surface has a statistically significant spatial relationship with the two Large Low Shear Velocity Provinces (LLSVPs) [e.g., Burke *et al.*, 2008; Austermann *et al.*, 2014; French and Romanowicz, 2015], indicating that LLSVPs may play a role in controlling dynamics within the convecting mantle. LLSVPs are thermally and/or chemically distinct features in the mantle that have on average 1–2% decrease in shear wave velocity from PREM; one lies beneath the Pacific and the other beneath Africa [e.g., Davies *et al.*, 2012]. The edges of the LLSVPs are seismically sharp as well [Ni *et al.*, 2002; Wang and Wen, 2007].

The role of downwelling material, such as subducted slabs that may impinge on the core-mantle boundary, should also be considered as another potentially important contributor to dynamic phenomenon in the D'' layer. For example, while diffusion creep may dominate the majority of the lower mantle, dislocation creep may localize near subducting slabs [McNamara *et al.*, 2001]. Subducting slabs may also stabilize postperovskite in D'' due to their lower temperatures than the surrounding mantle [e.g., Hernlund and Labrosse, 2007]. Subducted material also has the potential to introduce chemical heterogeneities in the lowermost mantle, where oceanic crust may accumulate. Sheets of subducted material can possibly accumulate at the base of the mantle in what are termed “slab graveyards,” as suggested by geodynamical modeling [Thomas *et al.*, 2004]. Lastly, there may be a strong link between the LLSVPs and subduction; geodynamical models can simulate the formation of thermochemical piles with geometries similar to LLSVPs by incorporating realistic subduction histories [e.g., McNamara and Zhong, 2005].

Interactions among subducted paleo-slabs, plumes, and LLSVPs likely represent important processes at the base of the mantle, but the nature of these interactions and the flow patterns that would be produced are still unclear. A few specific hypotheses for the pattern of flow at the base of the mantle have been articulated in the literature. Because the core-mantle boundary (CMB) represents a horizontal boundary layer, this flow should generally be horizontal, but there may be local exceptions. The downwelling motion of paleoslab material would likely produce nearly horizontal flow as slab material pushed ambient mantle to the side [e.g., McNamara *et al.*, 2002]; there may also be a component of pure shear or flattening with this type of motion. Three main hypotheses regarding the dynamics of LLSVPs and subducted material have been proposed [e.g., Hernlund and McNamara, 2015]: (1) active thermochemical LLSVPs may create buoyancy driven vertical flow [Davaille, 1999]; (2) passive thermochemical LLSVPs are dense piles that are swept around by slab remnants, associated with horizontal flow [e.g., McNamara and Zhong, 2005];

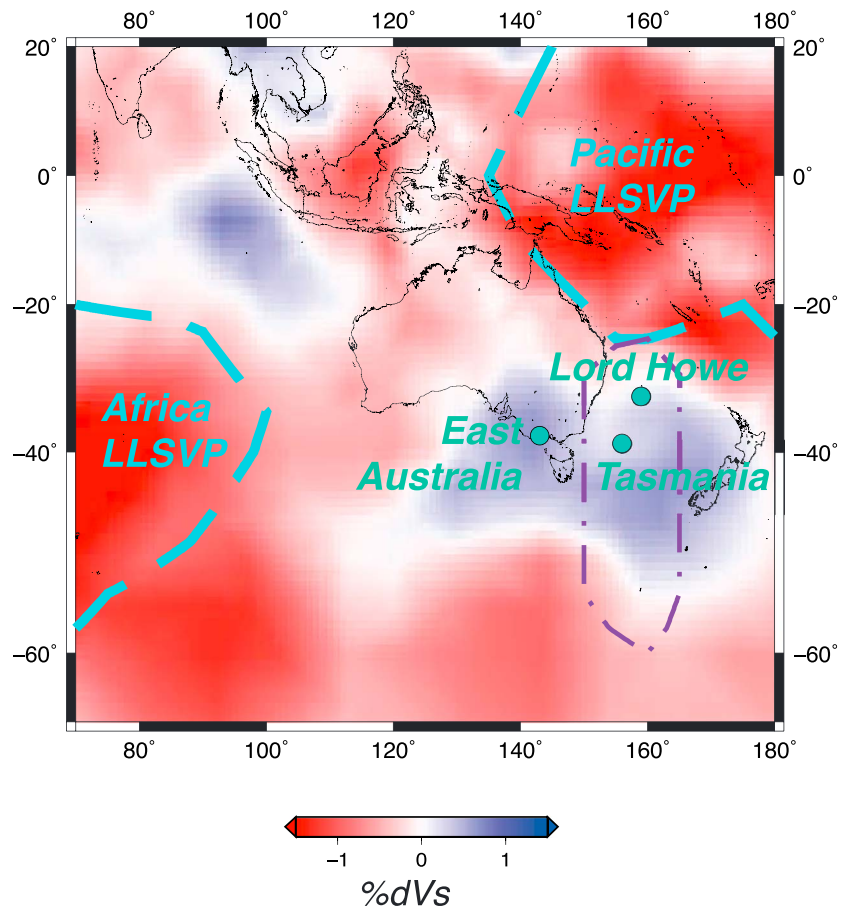


Figure 1. Map of study region. The background colors show the GyPSuM shear wave tomography model of *Simmons et al.* [2010] at a depth of 2650 km (250 km above the CMB), with velocity deviations indicated by the color bar. The locations of the Pacific and African LLSVP boundaries based on the cluster analysis of *Lekic et al.* [2012] are shown with cyan dashed lines. The green dots indicate the location of the East Australia, Tasmania, and Lord Howe hotspots, from *Steinberger* [2000a]. The purple line shows the inferred location of a higher than average density anomaly between 2300 to 2900 km depth, based on a model of past subduction rates and mantle flow [*Steinberger, 2000b*].

Hernlund and McNamara, 2015]; and (3) thermal LLSVPs may produce plumes at their edges, creating vertical flow [*Torsvik et al., 2006*].

The region beneath Australia is an excellent target area for studying the possible drivers of flow at the base of the mantle and is the geographic focus of this study. Our study region (Figure 1) lies between the boundaries of the African and Pacific LLSVPs, allowing us to potentially probe the character of anisotropy at the edges of these large-scale features. Our study region encompasses three hot spots (Lord Howe, Tasmania, and East Australia [*Steinberger, 2000a*]) that find expression in surface volcanism, ocean floor topography, and associated volcanic chains, and which may also be connected to structures in the lowermost mantle. It has been suggested that paleo-slab material may be present at the CMB in this region based on density anomalies calculated from dynamic modeling with past subduction models, particularly beneath New Zealand [*Steinberger, 2000b*]. The D" layer beneath the Antarctic Ocean and New Zealand is approximately ~350 km thick based on waveform modeling and traveltimes analysis [*Usui et al., 2005*]. The global average D" thickness is approximately 250 to 300 km, based on studies of various regions including Alaska [*Sun et al., 2016*], southeastern Asia [*Chaloner et al., 2009*], Russia [*Shen et al., 2014*], Central America [*Lay and Helmberger, 1983; Whittaker et al., 2015*], and the Indian Ocean [*Young and Lay, 1987*]. *Usui et al.* [2005] attribute the thicker than average D" beneath our study region due to the presence of paleo-slab material, in agreement with the inferences of *Steinberger* [2000b].

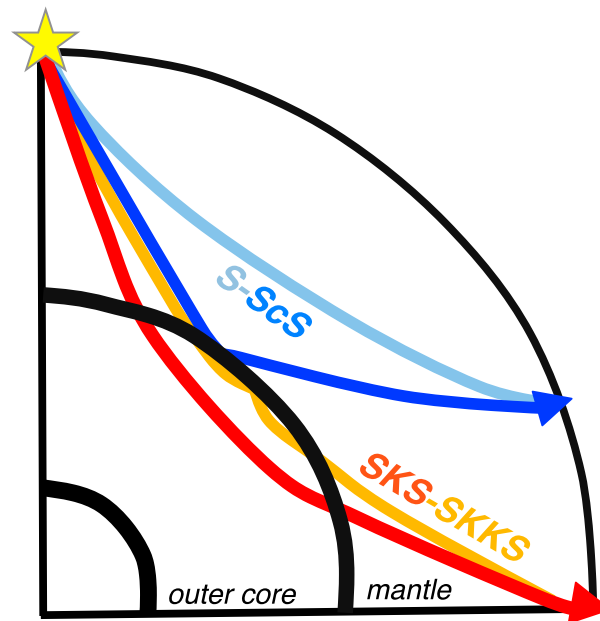


Figure 2. Diagram of raypaths used in this study for hypothetical event (star) and station (triangles) pairs. Raypaths for direct S (light blue), ScS (dark blue), SKS (red), and $SKKS$ (yellow) were calculated using TauP [Crotwell *et al.*, 1999] with the PREM velocity model [Dziewonski and Anderson, 1981].

Many published studies of D'' anisotropy using body waves have relied on observations for only one type of phase, typically over a limited number of azimuths (usually one), due to limitations imposed by source and receiver locations. This limited sampling typically means that the geometry of the anisotropy cannot be fully constrained. One increasingly common observational strategy relies on the combination of observations at multiple azimuths [e.g., Wookey *et al.*, 2005a; Wookey and Kendall, 2008; Nowacki *et al.*, 2010] and/or the combination of different types of phases [e.g., Ford *et al.*, 2015]. We follow this strategy in this study, combining differential S - ScS splitting [Wookey *et al.*, 2005a] and differential SKS - $SKKS$ splitting [e.g., Long, 2009] for a set of paths that sample the lowermost mantle beneath Australia over a range of propagation directions (Figure 2).

This choice of study region is advantageous because we can achieve suitable coverage (over several unique directions) by measuring events originating in the western Pacific and South American subduction zones at stations in and around Australia with previously documented weak or simple upper mantle anisotropy [Lynner and Long, 2013, 2014b; Mohiuddin *et al.*, 2015]. In this paper we present a set of shear wave splitting observations due to lowermost mantle anisotropy beneath Australia, as well as a set of forward modeling experiments that test a variety of elasticity scenarios and orientations in order to constrain the possible mechanisms and flow geometries. We implement the forward modeling approach of Ford *et al.* [2015], selecting a set of single-crystal elastic tensors for D'' materials as well as a set of elastic tensors based on polycrystalline plasticity modeling [Walker *et al.*, 2011] and testing all possible orientations. For each candidate orientation, we predict shear wave splitting for the raypath propagation directions contained in our data set, based on solutions to the ray theoretical Christoffel equation as implemented in the MSAT toolkit [Walker and Wookey, 2012].

2. Shear Wave Splitting Methods and Observations

2.1. Methodology

The widespread presence of seismic anisotropy in the upper mantle [e.g., Savage, 1999] presents challenges for isolating the contribution from anisotropy in the lowermost mantle. Combining different types of phases with similar paths in the upper mantle but different paths in the lower mantle commonly circumvents this challenge. Examples of this include the measurement of differential SKS - $SKKS$ splitting [e.g., Niu and Perez, 2004; Long, 2009] and the measurement of differential S - ScS splitting [Wookey *et al.*, 2005a] (Figure 2). For the case of SKS - $SKKS$, the conversion from a P wave to an S wave at the CMB means there is no contribution from anisotropy on the source side. The similar raypaths in the upper mantle allow the two phases to sample any upper mantle anisotropy in (nearly) the same way. If stations with a known contribution to $SK(K)S$ splitting from upper mantle anisotropy (as documented by previous investigations of $SK(K)S$ splitting over a range of back azimuths) are used, then explicit corrections for the effect of upper mantle anisotropy can be applied, and the contribution from the lowermost mantle can be isolated [e.g., Lynner and Long, 2014b; Long and Lynner, 2015]. This approach assumes that there is no significant contribution to anisotropy from the bulk of the lower mantle [e.g., Meade *et al.*, 1995]. Work by Usui *et al.* [2005] provides another constraint that

the lowermost mantle is largely anisotropic in our study region, as they found that shear wave anisotropy most likely begins approximately 350 km above the core mantle boundary.

In this study, we used permanent stations in and around Australia with well-studied and simple (or negligible) contributions to $SK(K)S$ splitting from upper mantle anisotropy. Specifically, we only used stations that overlie simple or weak upper mantle anisotropy, using the criteria of *Lynner and Long* [2013] to identify stations with one of two patterns of upper mantle anisotropy: (1) a pattern of null $SK(K)S$ arrivals from many different back azimuths with few split arrivals or (2) a splitting pattern for which splitting measurements are similar across multiple back azimuths. For the first type of pattern, no correction is needed. For stations with the second type of observed pattern of upper mantle anisotropy, a correction is applied to all S , ScS , SKS , and $SKKS$ waveforms by rotating and time shifting the horizontal components [*Lynner and Long*, 2013] using the parameters associated with splitting due to upper mantle anisotropy.

We carried out SKS and $SKKS$ measurements using the SplitLab software [*Wüstefeld et al.*, 2008], which implements a grid search to find the best combination of delay time and fast direction using three different measurement methods: transverse energy minimization, rotation correlation, and minimum eigenvalue methods [e.g., *Silver and Chan*, 1991]. We identified SKS and $SKKS$ phases from the same station-receiver pairs, removed the contribution to splitting from upper mantle anisotropy as described above, and then measured the splitting of the corrected waveforms using SplitLab. We only retained measurements for which the transverse energy minimization and rotation correlation measurement methods agreed (within the 2σ errors). Measurements presented here represent the average of these two methods for $SK(K)S$.

For differential S - ScS splitting [*Wookey et al.*, 2005a], we take advantage of the similarity in raypaths in the upper mantle on both the source and receiver side to isolate the contribution to ScS splitting from the D'' layer (Figure 2). We consider three potential sources of anisotropy that may contribute to the splitting of ScS phases: the upper mantle near the source, the D'' layer, and the upper mantle beneath the receiver. We apply upper mantle corrections to both the S and ScS waveforms based on previously published SKS corrections at the stations [*Lynner and Long*, 2013, 2014b; *Mohiuddin et al.*, 2015], as with the differential SKS - $SKKS$ measurements. After applying the receiver side correction, the splitting of the direct S phase reflects the contribution from anisotropy near the earthquake source. We measured these splitting parameters associated with anisotropy on the source side of the raypath and incorporated them into the grid search for the D'' splitting, inferred from the ScS phase. We implemented a grid search alongside SplitLab for the best fitting shear wave splitting parameters due to lowermost mantle anisotropy, similar to *Wüstefeld et al.* [2008]. To solve for the D'' -associated splitting parameters, we searched over all possible delay times up to 6 s and fast directions. At each point in the grid search, we corrected the waveforms with each candidate set of splitting parameters for D'' splitting and then applied the correction for source side splitting. Using the resulting corrected waveforms, we computed the minimum second eigenvalue based on the eigenvalue measurement method [*Silver and Chan*, 1991] and the maximum cross-correlation coefficient of the (corrected) horizontal components. This measurement strategy, developed by *Wookey et al.* [2005a], corrects the waveforms in the reverse order in which the ray has traveled through the Earth, in order to account for the noncommutative behavior of the shear wave splitting operators [e.g., *Silver and Savage*, 1994; *Silver and Long*, 2011]. An example of a differential S - ScS splitting measurement is shown in Figure 3. The ScS results given in this study are an average of the measured D'' -associated splitting parameters for the two measurement methods (that is, the eigenvalue method and the rotation-correlation method).

2.2. Data Selection and Processing

We selected 10 long-running stations for analysis, mostly from the Global Seismographic Network, located in Australia, Antarctica, New Zealand, and the Arctic (Figure 4). Each of these stations exhibits simple splitting patterns for SKS phases (as documented by *Lynner and Long* [2013, 2014b] and *Mohiuddin et al.* [2015]), according to the criteria described above. The corrections for upper mantle anisotropy beneath the stations are shown in Tables S1 and S2. For SKS - $SKKS$, we selected events for analysis with magnitude greater than 5.5 at epicentral distances between 108° and 120° ; at these distances, both SKS and $SKKS$ phases are commonly visible [e.g., *Niu and Perez*, 2004]. For S - ScS , we selected events with magnitude greater than 5.5 at epicentral distances between 60° and 80° , following *Wookey et al.* [2005a]. We applied a band-pass filter with corner periods of 8 and 25 s to all waveforms to achieve consistency with previous studies of upper mantle anisotropy at

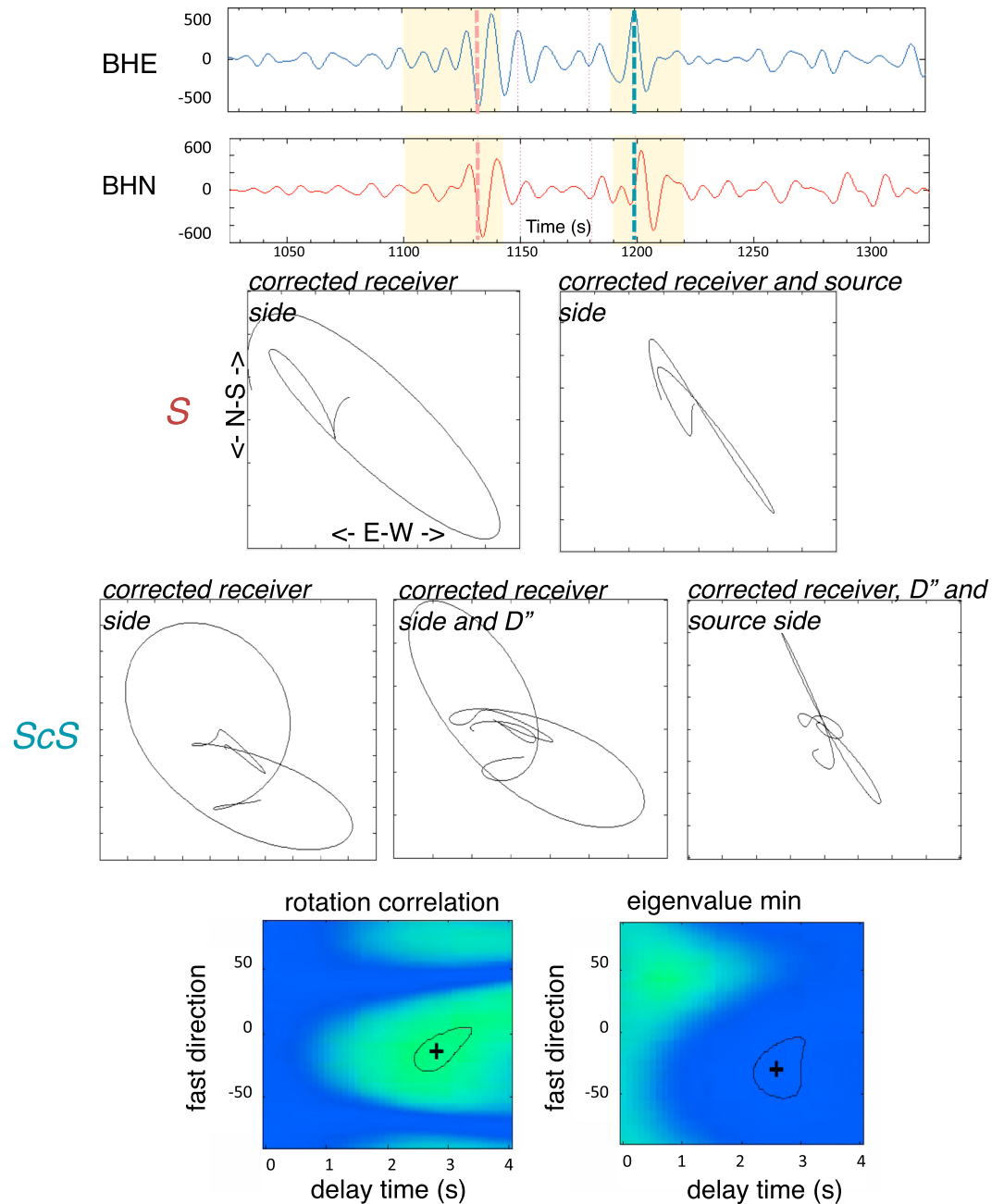


Figure 3. Example of an S-ScS splitting measurement for D'' anisotropy. (first row) The band-pass filtered (8 to 25 s) and uncorrected horizontal seismic waveforms along with the predicted S (red) and ScS (blue) arrival times based on PREM. The yellow region shows the time window used for the splitting analysis. (second row) The particle motion diagrams (with up-down corresponding to north-south, and left-right corresponding to east-west) for the direct S phase after correction for receiver side anisotropy (left) and after correction for both source and receiver side anisotropy, where the receiver side correction is made first (right). (third row) The particle motion diagrams for ScS after correction for receiver side anisotropy (left), after correction for receiver side anisotropy and D'' anisotropy using the best fitting splitting parameters from the grid search (middle), and after correction for anisotropy near the receiver, D'', and the source side (right). For both S and ScS, the particle motion is linear after correction for all anisotropic regions. (fourth row) The grid search results for D'' anisotropy for the two measurement methods used with the best fitting splitting parameters shown with a cross and the black line indicating the 95% confidence region. The rotation correlation method searches for the maximum correlation value between the two horizontal components (left image, where green is large and blue is low). The eigenvalue minimization method tries to minimize the smaller eigenvalue; therefore, the best solution (black cross) is within the minimum of the grid search map (right image, where green is large and blue is low).

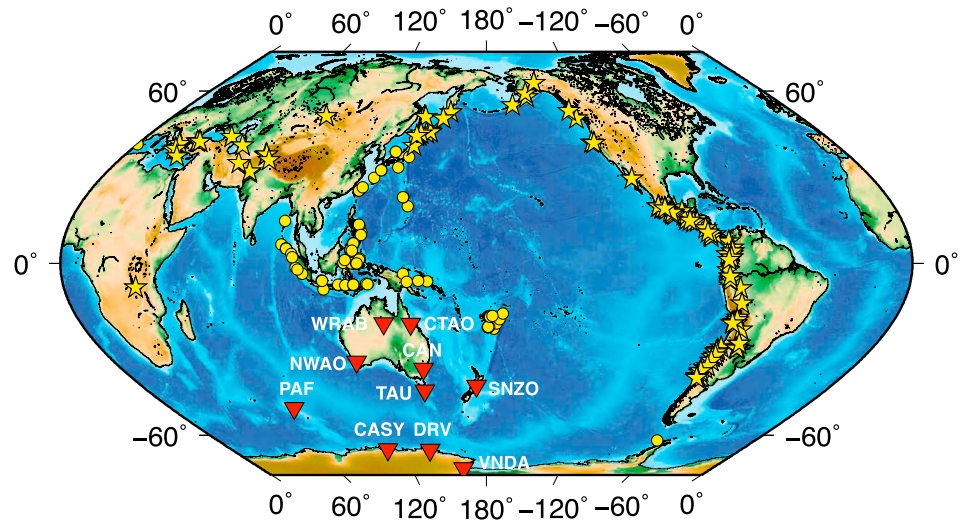


Figure 4. Map of events and stations (red triangles) used in this study. Earthquakes for which *SKS-SKKS* measurements were made are shown with a yellow star, while events that were used for the *ScS-S* analysis are shown with yellow circles.

these stations. Seismograms were inspected manually for high signal-to-noise ratio and good waveform clarity and were manually windowed for splitting analysis.

2.3. Shear Wave Splitting Results

Our measurement procedure yielded a total of 103 well-constrained pairs of *SKS-SKKS* splitting measurements, with 14 of these (14%) exhibiting significant discrepancies between *SKS* and *SKKS*, arguing for a contribution from lowermost mantle anisotropy. For all of the remaining phases, both *SKS* and *SKKS* were null (that is, nonsplit), indicating a lack of contribution from the lower mantle. For those measurements that were split, delay times ranged from 0.5 to 2.5 s. We obtained 72 measurements of *D''*-associated splitting from *ScS* phases; of these, 28% were null and the rest split. *D''*-associated delay times for *ScS* ranged from 0.5 s to 5.1 s, with an average δt of 2 s; these larger delay times for *ScS* compared to *SK(K)S* likely reflect the longer raypaths through *D''* (200–600 km for *SKS/SKKS* versus 1200–1400 km for *ScS*). Tables S1 and S2 contain each of the individual splitting measurements made in this study.

Our measurements are shown in map view in Figures 5 and 6, for which we have calculated raypaths through a 250 km thick *D''* region for the PREM velocity model using TauP [Crotwell *et al.*, 1999] and plotted the *D''*-associated splitting parameters for each phase at the midpoint of the *D''* raypath. These maps (*SKS-SKKS* measurements in Figure 5 and *ScS* measurements in Figure 6) demonstrate evidence for significant but laterally variable splitting due to lowermost anisotropy in our study region. The majority of *SK(K)S* null measurements sample beneath Australia and near the LLSVP edges, while the majority of the split measurements sample the lowermost mantle outside of the LLSVPs and beneath the southern Antarctic Ocean, Antarctica, or Indonesia. While there is some scatter in measured fast directions for individual locations, they are generally consistent within individual groups with similar raypaths, providing confidence in our observations. In regions where we identified significant *ScS* splitting, it was often the case that *SK(K)S* phases sampling those regions appeared to be null (nonsplit). This difference may be due to the difference in path length through *D''*, with *SK(K)S* phases having shorter path lengths (200–500 km) than *ScS* (1000–1500 km) and thus potentially experiencing less splitting. Alternatively, it may reflect an anisotropic geometry that would yield splitting of horizontally propagating waves, while phases with a more vertical orientation may not be split. Each of these two possibilities is accommodated by our forward modeling framework, discussed in section 3 below.

The majority of the *ScS* measurements exhibits splitting and mostly sample beneath New Zealand, Australia, and the border of the Pacific LLSVP. The few clusters of null *ScS* measurements are located beneath Indonesia and east of New Zealand. In general, there is consistency among fast direction observations except for the occasional null measurement and observations in the Indian Ocean off the western coast of Australia, which

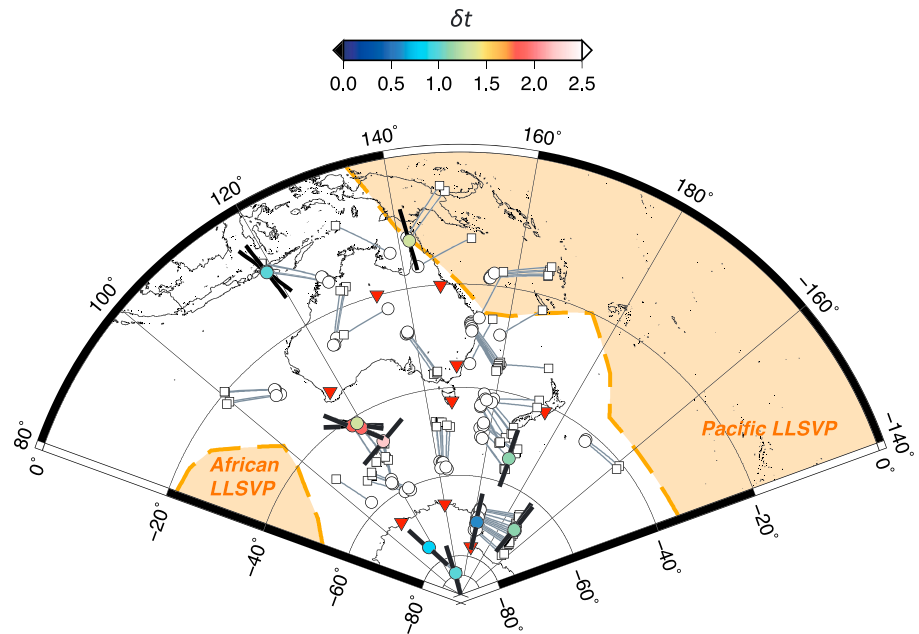


Figure 5. Map of SKS-SKKS splitting measurements. SKS (circles) and SKKS (squares) splitting parameters (after correction for the effect of upper mantle anisotropy) are plotted at their CMB exit point, calculated using TauP [Crotwell *et al.*, 1999]. The black bars indicate the splitting parameters for split measurements (orientation of the bar corresponds to fast direction; symbol color indicates delay time as shown by the color bar), measured in the geographic reference frame of the station. Null measurements are shown as white symbols. The light gray lines connect SKS and SKKS phases for the same event-station pair. The light brown shaded regions indicate the African and Pacific LLSVPs, from the cluster analysis of Lekic *et al.* [2012].

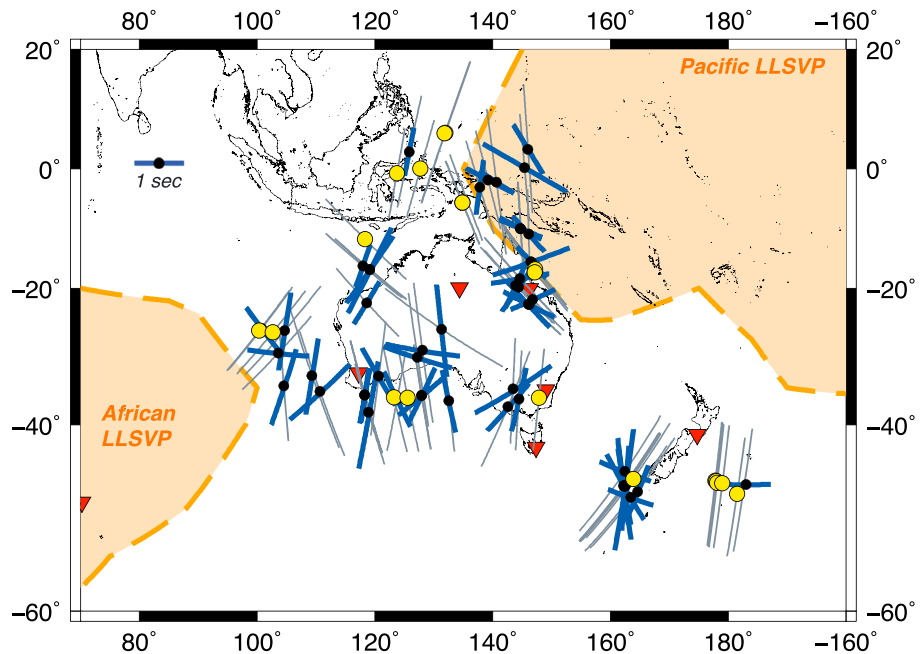


Figure 6. Map of ScS splitting measurements. Measurements are plotted at the midpoint of the D'' path (light gray lines), as calculated for a 250 km thick layer using TauP [Crotwell *et al.*, 1999]. The blue bars with black dots indicate D''-associated splitting parameters, with the orientation of the bar indicating the fast direction (as measured at the station) and the length indicating delay time. The yellow dots designate null measurements. The light orange regions indicate the African and Pacific LLSVPs, as delineated by Lekic *et al.* [2012].

show a high degree of scatter. This scatter might be due to poor data quality, since the inconsistent measurements were all recorded at an ocean island station, PAF, and were not used in the forward modeling component of our study. While fast directions appear to be generally consistent within regions, delay times vary considerably within regions. In general, delay times appear to be larger in the south of the study region and smaller in the northern part of the study region.

Based on the data set shown in Figures 5 and 6, we have identified two subregions within our study area for further analysis and forward modeling, one beneath New Zealand (Figure 7) and one beneath southwestern Australia (Figure 8). Each of these subregions is sampled over at least four distinct propagation directions, with multiple (consistent) measurements for each direction. Furthermore, for each of these subregions there is evidence for the presence of anisotropy, as at least some of the paths exhibit consistent splitting. As described in section 3, we apply a forward modeling strategy to each of these subregions individually to obtain constraints on the mechanism and orientation of anisotropy. Table 1 lists the average splitting measurements for each group of raypaths for each of the two subregions.

3. Mineral-Physics Based Forward Modeling: Approach and Results

3.1. Forward Modeling Approach

All of the major mineral components of the lower mantle, including magnesium silicate perovskite or bridgmanite (PV), ferropericlase (Mg, Fe)O (Fp), and the high pressure polymorph of bridgmanite, postperovskite (PPV), have significant single-crystal anisotropy, as demonstrated by ab initio calculations [e.g., Karki *et al.*, 1999]. In this study we test both LPO and SPO scenarios for anisotropy; specifically, we examine scenarios that invoke single-crystal elasticity or textured aggregates (for MgO and PPV [Long *et al.*, 2006; Walker *et al.*, 2011]) as well as a variety of SPO scenarios that invoke aligned inclusions of partial melt [Walker and Wookey, 2012]. Our method for forward modeling follows Ford *et al.* [2015], who applied the technique to a data set that samples the lowermost mantle beneath the Afar peninsula along the edge of the African LLSVP. Here we apply a similar modeling approach to the New Zealand and SW Australia subregions of our data set. The goal of the modeling is to compare predictions of shear wave splitting for a suite of possible elastic tensors, over the full range of possible orientations, to the path-averaged D'' -associated splitting parameters for SKS, SKKS, and ScS (Table 1 and Figures 7 and 8).

Because the dominant slip systems and thus LPO patterns in lowermost mantle minerals remain imperfectly known, we test scenarios based on both single-crystal elasticity (hypothesizing that the pattern, although not the strength, of anisotropy will be similar for a single crystal and a deformed aggregate) and on predictions of likely texture. Following Ford *et al.* [2015], we tested a variety of single-crystal elastic tensors based on ab initio calculations at a range of temperature conditions for Fp, PV, and PPV (Table 2) [Karki *et al.*, 1999; Wookey *et al.*, 2005a, 2005b; Stackhouse *et al.*, 2005; Wentzcovitch *et al.*, 2006]. For some of the mineralogical scenarios considered from a single-crystal perspective, we also tested tensors that are meant to represent more realistic LPO scenarios for the lower mantle. For Fp, we tested an elastic tensor for MgO from Long *et al.* [2006] that was derived from a combination of an experimentally determined LPO pattern at relatively low pressure (300 MPa) and a temperature of 1473 K with single-crystal elastic constants calculated for lowermost mantle pressures. For PPV, we tested elastic tensors derived from the global model TX2008 V1 of 3-D mantle flow with PPV texture modeling from the work of Walker *et al.* [2011]. Specifically, we selected a region of the model that exhibits horizontal simple shear at the base of the mantle, with a known shear direction, and used predicted elastic tensors assuming three different dominant slip systems for PPV. Lastly, we tested two SPO scenarios based on aligned partial melt in different geometries. SPO elastic tensors were calculated using effective medium theory as implemented in MSAT [Walker and Wookey, 2012] for which the P and S wave velocities of the matrix are 13.9 km/s and 7.9 km/s, respectively; density of matrix is 5324 kg/m³, the P and S wave velocities of the inclusion are 7 km/s and 0 km/s, respectively; the two aspect ratios tested are 0.01 (oblate) and 100 (tubule); and the volume melt fraction is 0.003.

Our modeling approach makes several assumptions, as discussed in Ford *et al.* [2015]. First, we assume that the anisotropic structure is laterally homogenous within each of our subregions, and thus that each of the individual raypaths is sampling the same anisotropy. For our single-crystal elasticity scenarios, we make the assumption that a textured aggregate will have an anisotropic geometry that is similar to a single crystal. This approach overestimates the anisotropic strength; however, we overcome this limitation by considering

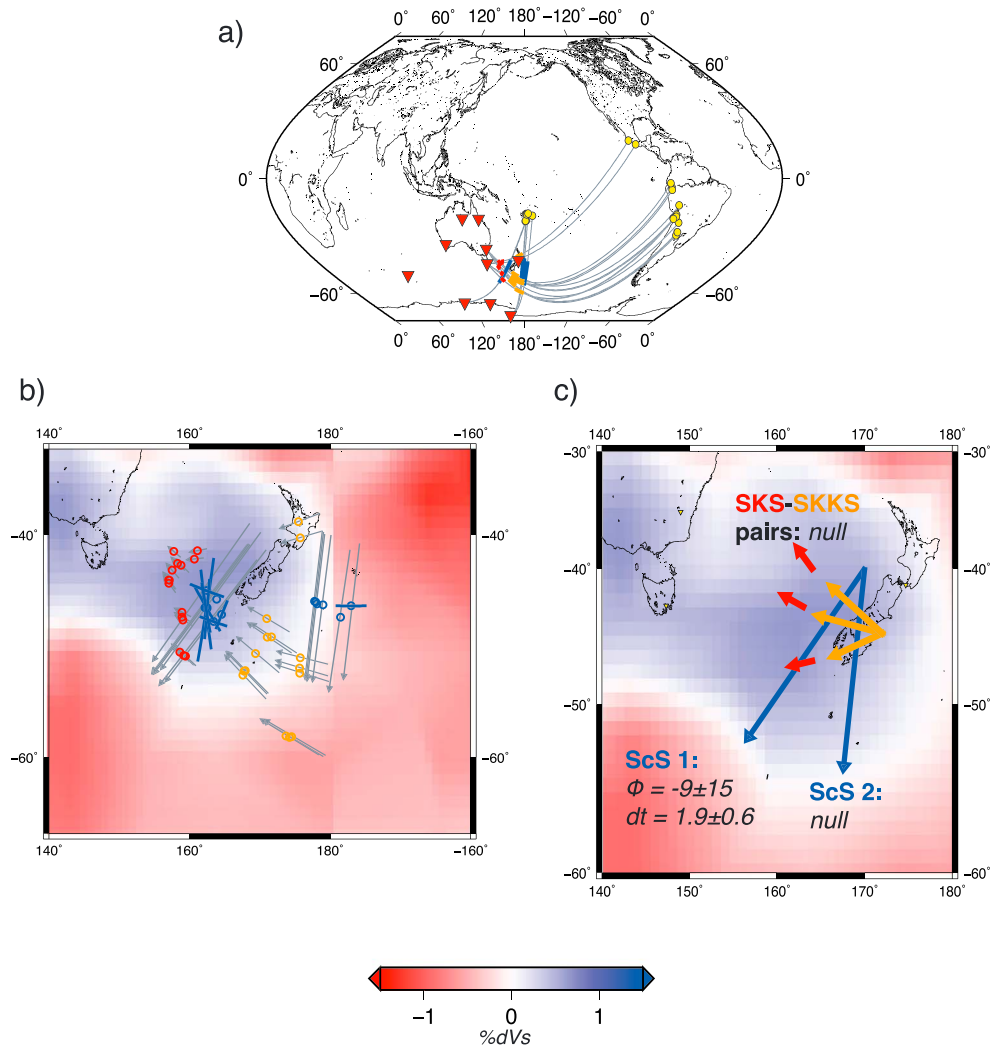


Figure 7. Summary of observations for the New Zealand subregion. (a) Raypaths and earthquake-receiver pairs for ScS (blue), SKS (red), and SKKS (orange) with the corresponding raypaths (light black lines) through the D'' layer. This subregion encompasses two groups of ScS propagating to the south and southwest, as well as three pairs of SKS and SKKS paths with propagation directions ranging from west-southwest to northwest. (b) Individual splitting measurements for this region, including nulls (open circles) and splits (blue bars) as measured at the stations. The light gray lines show the raypaths through D'', with the arrow indicating the direction of propagation. The background colors indicate lowermost mantle shear velocities from the GyPSuM model 250 km above the CMB (as shown in the color bar). (c) Schematic view of the path-averaged splitting parameters used in the forward modeling, as shown in Table 1. Background colors are as in Figure 7b.

relative rather than absolute delay times, as discussed below. Finally, our modeling approach implements ray theory, and we do not consider finite frequency effects, which may be significant for realistic lowermost mantle anisotropy scenarios that include lateral heterogeneity [Nowacki and Wookey, 2016].

We calculated an average straight line approximation of each path for every set of rays through the D'' layer, assuming an anisotropic layer thickness of 350 km. For SKS and SKKS, we calculated incidence angles of each group of rays using TauP [Crotwell et al., 1999] with the ak135 velocity model [Kennett et al., 1995]. For ScS, we assumed horizontal propagation through D''; this is a common assumption [e.g., Nowacki et al., 2010; Ford et al., 2015], although propagation angles can vary from the horizontal up to 15°. We transformed the splitting parameters into a ray-centered coordinate system, following Nowacki et al. [2010].

For each subregion, we tested 14 individual elastic tensors (Table 2) over a range of orientations, with the tensor rotated in 5° increments around each of the three rotation axes. Predicted splitting parameters

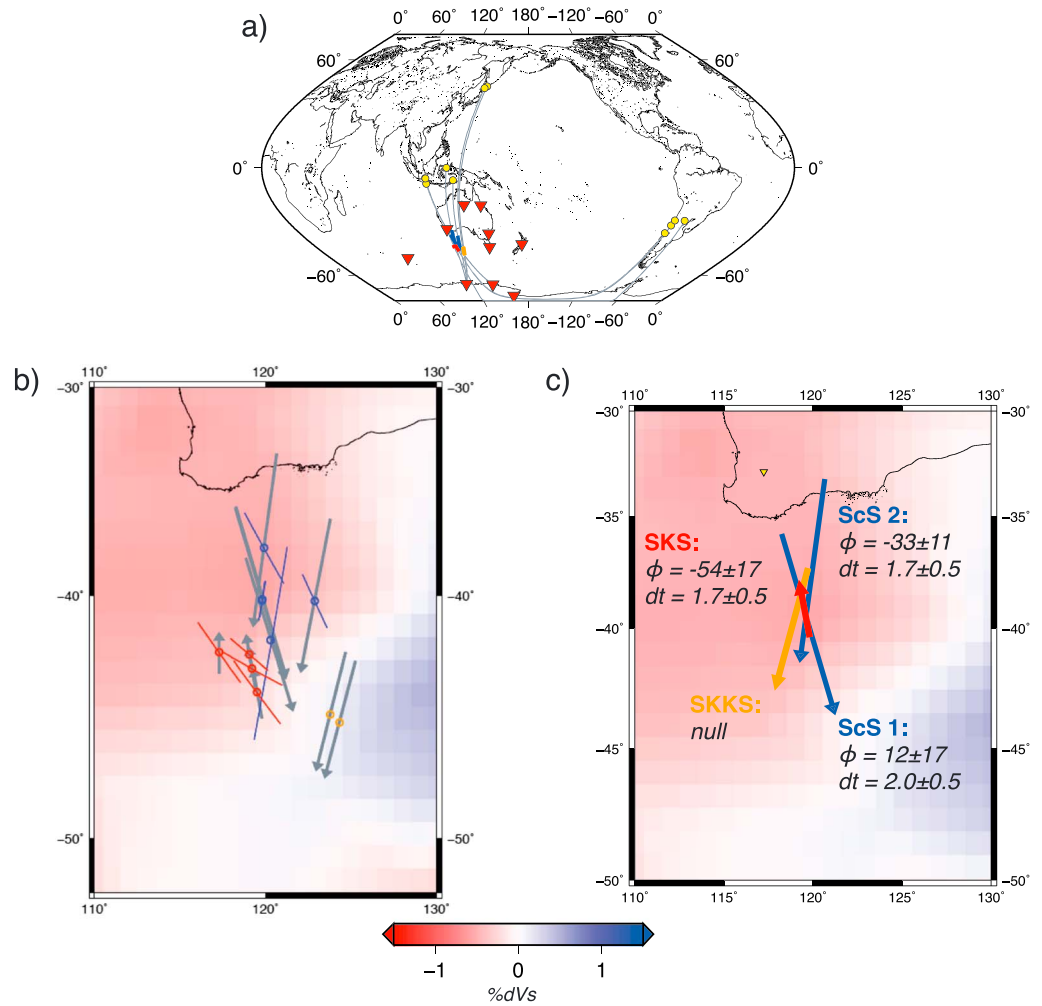


Figure 8. Summary of observations for the southwest Australia subregion. Plotting conventions are as in Figure 7.

(fast directions and delay times) for each set of rays were calculated by solving the Christoffel equation using the MSAT toolkit [Walker and Wookey, 2012]. For each candidate tensor and orientation under consideration, we rejected the model if it predicted any fast direction that was more than 20° away from the observation or if it incorrectly predicted a null observation, as described below. For models

Table 1. Raypath-Averaged Splitting Parameters for Each Group of Phases for Each of the Two Subregions Selected for Forward Modeling^a

Phase	ϕ	$\pm\phi$	δt	$\pm\delta t$	Azimuth
<i>New Zealand</i>					
ScS 1	-9	15	1.9	0.6	261
ScS 2	NA	NA	Null	NA	203.6
SKS-SKKS 1	NA	NA	Null	NA	324.1
SKS-SKKS 2	NA	NA	Null	NA	270.5
SKS-SKKS 3	NA	NA	Null	NA	315.1
<i>Southwestern Australia</i>					
ScS 1	12	17	2	0.5	146.7
ScS 2	-33	11	1.7	0.5	198.3
SKS	-54	17	1.7	0.5	353.9
SKKS	NA	NA	Null	NA	205.8

^aColumns show the geographic region, the phase type, the average fast direction (degrees from N), the average 95% confidence range on the fast direction estimate, the average delay time (seconds), the average 95% confidence range on the delay time estimate, and the average azimuth of the group of rays.

Table 2. Summary of All Elastic Tensors Used in the Forward Modeling^a

Geometry	Phase	Pressure (GPa)	Temperature (K)	References
<i>Single Crystal Tensors</i>				
	PV	125	2500	<i>Wentzcovitch et al. [2006], Wookey et al. [2005a, 2005b]</i>
		126	2800	
		136	4000	
	PPV	136	3000	<i>Stackhouse et al. [2005], Wentzcovitch et al. [2006]</i>
		135	4000	
		125	2500	
		140	4000	
	Fp	135	3000	<i>Karki et al. [1999]</i>
<i>Other Tensors</i>				
		Notes		
Experimental LPO	MgO	$P = 0.3 \text{ GPa}; T = 1473 \text{ K}$		<i>Long et al. [2006]</i>
SPO	0.003 vol. fraction melt	Oblate shape		<i>Walker and Wookey [2012]</i>
	0.003 vol. fraction melt	Tubule shape		<i>Walker and Wookey [2012]</i>
Calculated LPO	PPV	TX2008-V1 model; 3 dominant slip planes tested: (001) (010) (100); $P = 125\text{--}136; T = 3000\text{--}4000 \text{ K}$		<i>Walker et al. [2011]; Tensors based on Stackhouse et al. [2005] and Stackhouse and Brodholt [2007]</i>

^aFor the single-crystal tensors, the pressure and temperature conditions used in the modeling are also indicated. Columns show the type of tensor (single-crystal, LPO based on experimental data, SPO based on effective medium averaging, or LPO based on global flow and texture models), the phase and/or constituents, and the reference.

that were not discarded and considered an acceptable fit to the data, we calculated a misfit value based on a residual sum of squares approach, following *Ford et al. [2015]*. Each misfit for relative delay time and fast direction were summed and weighted such that the delay time misfits are normalized by the half of the maximum delay time and fast direction misfits are normalized by the maximum residual of 90°. The expression for the residual is given by the following equation, in which n is the number of observations, y is each observation (fast direction or delay time), and $f(x)$ are the predictions for each corresponding observation:

$$\text{Residual sum of squares} = \sum_{i=1}^n (y_i - f(x_i))^2 \quad (1)$$

Delay times are a function of anisotropic strength and path length. In order to avoid making any assumptions about anisotropic strength, we calculate relative delay times, based on an assumption of a 350 km thick anisotropic layer (using the D" discontinuity depth for our study region from *Usui et al. [2005]*). The calculation for delay time and relative delay time is defined below:

$$\text{Relative delay time (RDT)} = \frac{\delta t_M - \delta t_N}{(\delta t_M + \delta t_N)/2} * 100 \quad (2)$$

$$\delta t_{\text{pre}} = T * \left(\frac{1}{v_{\text{slow}}} - \frac{1}{v_{\text{fast}}} \right) \quad (3)$$

Here T , δt_M , and δt_N represent the total path length through the D", the predicted delay time calculated in equation (3), and observed delay time, respectively. This equation for RDT is applied for both the observed and predicted delay times. These equations are applied for every observation at every possible orientation for each tested elastic tensor.

The treatment of null (that is, nonsplit) measurements in the forward modeling is an important consideration. A null measurement could be either due to weak or nonexistent anisotropy, or it could result from the alignment of the initial polarization of the incoming wavelet with the fast or slow directions of anisotropic symmetry. We directly measured the initial polarizations from the waveform for all null ScS waves, following the method of *Vidale [1986]*. For SK(K)S phases, the polarization is constrained to be equivalent to the back

Table 3. Summary of Forward Modeling Results^a

	New Zealand	Southwestern Australia
Fp	yes ^b	no
MgO LPO	no	yes ^b
PPV(125,2500)	yes ^c	yes ^b
PPV(135,4000)	yes ^c	yes ^b
PPV(136,3000)	yes ^c	yes ^b
PPV(140,4000)	yes ^c	no
PV(125,2500)	yes ^c	no
PV(126,2800)	yes ^b	no
PV(136,4000)	yes ^b	no
SPO Tubule	no	no
SPO Oblate	yes ^b	no
<i>TX2008 V1-LPO models PPV</i>		
(001)	yes ^c	no
(010)	yes ^b	yes ^b
(100)	no	no

^aFor each elastic tensor under consideration, the table lists whether our modeling successfully identified an orientation that fit the observations for each subregion. For the successful scenarios, we also indicate how the null observations fit the predictions (alignment with initial polarization direction^c or predicted weak anisotropy^b).

^bAll null measurements due to weak anisotropy.

^cNull measurement (ScS null for New Zealand and SKKS null for SW Australia) aligned with back azimuth.

azimuth by the *P*-to-*S* conversion at the CMB and is the same for the entire group of rays. Our modeling approach takes into account both possible scenarios for the null observations, again following *Ford et al.* [2015]. For paths along which we observe only null measurements, we take into account the possibility of weak anisotropy by implementing a cutoff of 0.5 s delay time, which represents a typical error on a delay time measurement (put another way, our observational strategy cannot constrain splitting with a delay time of less than 0.5 s). If there is a large spread in the initial polarizations, then the null measurements could be due to weak or absent anisotropy; however, if the initial polarization directions for a given set of measurements are similar, we must test both possible explanations. The 0.5 s cutoff, in which a model is discarded if it predicts more than 0.5 s of splitting for a path that exhibits no splitting in the data, is applied after a linear scaling of the predicted delay times to match the nonnull observations in the data set for each subregion. We consider a prediction to successfully match a null observation if either (1) the predicted (scaled) delay time is less than the 0.5 s cutoff or (2) the predicted fast or slow direction is within 20° of the initial polarization (ScS) or the back azimuth (SK(K)S) direction. For ScS phases, a set of null observations along a single path can be considered to correspond to weak or absent splitting if there is a sufficiently large spread in initial polarization directions in the data to rule out the possibility that the null measurements are due to the alignment of the initial polarization direction to a fast or slow direction of anisotropy; otherwise, this possibility is considered in the modeling.

azimuth by the *P*-to-*S* conversion at the CMB and is the same for the entire group of rays. Our modeling approach takes into account both possible scenarios for the null observations, again following *Ford et al.* [2015]. For paths along which we observe only null measurements, we take into account the possibility of weak anisotropy by implementing a cutoff of 0.5 s delay time, which represents a typical error on a delay time measurement (put another way, our observational strategy cannot constrain splitting with a delay time of less than 0.5 s). If there is a large spread in the initial polarizations, then the null measurements could be due to weak or absent anisotropy; however, if the initial polarization directions for a given set of measurements are similar, we must test both possible explanations. The 0.5 s cutoff, in which a model is discarded if it predicts more than 0.5 s of splitting for a path that exhibits no splitting in the data, is applied after a linear scaling of the predicted delay times to match the nonnull observations in the data set for each subregion. We consider a prediction to successfully match a null observation if either (1) the predicted (scaled) delay time is less than the 0.5 s cutoff or (2) the predicted fast or slow direction is within 20° of the initial polarization (ScS) or the back azimuth (SK(K)S) direction. For ScS phases, a set of null observations along a single path can be considered to correspond to weak or absent splitting if there is a sufficiently large spread in initial polarization directions in the data to rule out the possibility that the null measurements are due to the alignment of the initial polarization direction to a fast or slow direction of anisotropy; otherwise, this possibility is considered in the modeling.

3.2. Forward Modeling Results

3.2.1. New Zealand Subregion

The New Zealand data set (Figure 7) encompasses eight distinct raypath directions; of these, seven are non-split, and one (associated with ScS phases propagating to the south-southwest) exhibits splitting. We attempted to match this set of observations by testing all possible orientations of the elastic tensors shown in Table 2. Of the 14 elastic tensor scenarios tested, we found that all of the PPV tensors, the Fp elastic tensor, and all three PV tensors fit the data at one or more orientations, as well as the oblate SPO elastic tensor. We also identified elasticity scenarios based on PPV LPO that provided an acceptable fit to the observations, but only for those tensors that invoke dominant slip on the (001) or (010) planes. For the remaining candidate elastic tensors, we were unable to find an orientation that correctly predicted the observed splitting for all eight paths in the data set. This includes the MgO LPO tensor and the tubule SPO scenarios, suggesting that these anisotropic models are not appropriate for the region beneath New Zealand. Table 3 summarizes our modeling results for this subregion.

We were able to identify plausible orientations that fit the observations beneath New Zealand for all single-crystal PPV elastic tensors. An example of a successful PPV model for the New Zealand data set is shown in Figure 9. For these successful fits, the null ScS path (propagation to the south) must have an initial polarization direction aligned with either a fast or slow direction; weak anisotropy cannot explain this observation. In this case, the group of null ScS has little spread in the initial polarization values; therefore, we could not rule out the possibility of an alignment with the fast or slow direction. The null measurements for SKS and SKKS correspond to directions for which weak or absent splitting would be predicted by the model (red colors in

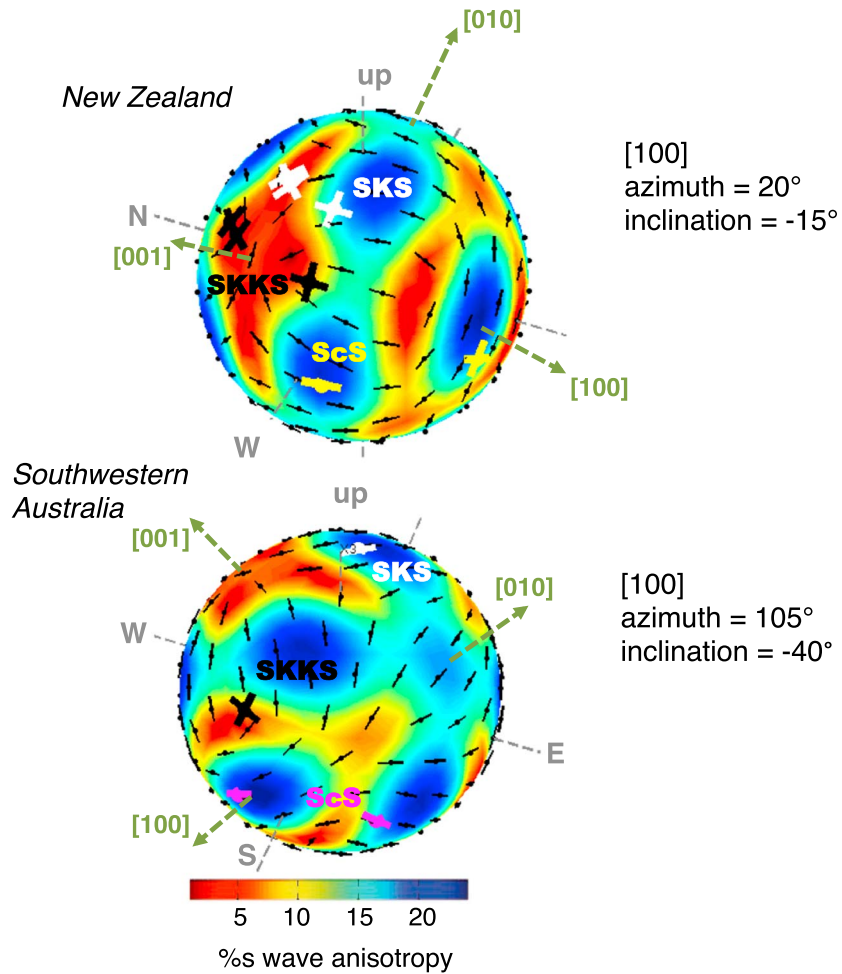


Figure 9. Examples of successful model fits for a single-crystal PPV elastic tensor [Stackhouse *et al.*, 2005]. (top) A successful fit for the New Zealand subregion. (bottom) A successful fit for the southwest Australia subregion. Predicted anisotropy is shown in a spherical representation relative to geographic space, with the east, north, west, and vertical directions indicated. The thin black lines show predicted splitting for different raypath directions. The colors indicate the percentage of shear wave anisotropy. The thick lines indicate the shear wave splitting observations for *SKS* (white), *SKKS* (black), and *ScS* (yellow or magenta). Null measurements are represented by crosses, in which the arms are oriented parallel and perpendicular to the initial polarization direction (*ScS*) or back azimuth (*SKS* and *SKKS*). The green dashed lines show the orientation of the [100], [010], and [001] crystallographic axes, according to the labels. For New Zealand, the orientation of the elastic tensor is such that the azimuth (from north) of the [100] crystallographic axis is 20° and its inclination (from the horizontal) is -15°. For southwest Australia, the orientation is such that that the azimuth (from north) of the [100] crystallographic axis is 105° and its inclination is -40°. Note that for New Zealand, the *SKS* and *SKKS* nulls propagate at directions for which the elasticity model predicts weak anisotropy, while the *ScS* null propagates such that the initial polarization is aligned with the predicted fast direction.

Figure 9a). A cluster analysis of the regions of orientation space with the lowest misfit [see Ford *et al.*, 2015], corresponding to the top 10% of acceptable models, allow us to evaluate the best fitting orientations for each of the three PPV tensors that successfully match the data. These orientations are shown in geographic space in Figure 10 (left column). The best fitting orientations are nearly identical for each PPV model; therefore, we only show solutions for one model. For New Zealand, just one cluster of possible azimuths and inclinations fit the observed data. This orientation involves a [100] axis that is close to horizontal, with an azimuth of about N15°E, while the [010] and [001] axes are oblique.

The three elastic tensors for PV that we tested also fit the data, with an example shown in Figure 11. For the successful PV models, we find that all of the null paths (*SKS*, *SKKS*, and *ScS* propagating to the south) propagate along orientations for which weak or absent splitting is predicted. The best fitting orientations for each

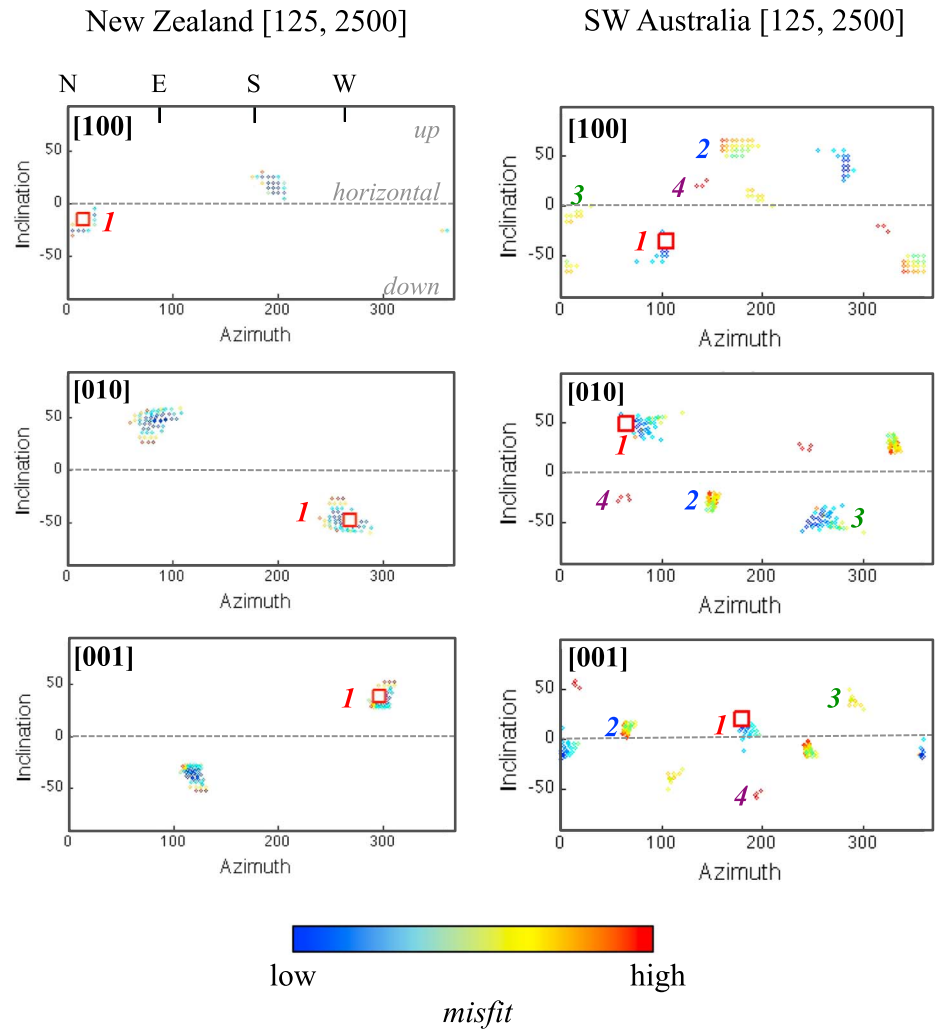


Figure 10. Best fitting orientations in geographic coordinates for single-crystal PPV (at 125 GPa and 2500 K [from *Wentzcovitch et al., 2006*]) for both subregions. Symbols indicate all of the orientations with acceptable fits for the (top row) [001], (middle row) [010], and (bottom row) [001] crystallographic axes of PPV in geographic space for (left column) southwestern Australia and (right column) New Zealand. The highlighted red squares indicate the minimum misfits (that is, the best fitting orientation). Each cluster, which represents a distinct azimuth (x axis) and inclination from the horizontal (y axis), is labeled with a number. Beneath New Zealand, we identify a single distinct orientation that fits the observed data. For southwestern Australia, we identify four distinct possible orientations that fit the observed data; where each cluster is ranked based on the minimum misfit (1 = lowest misfit, 4 = largest misfit). Azimuth is in degrees clockwise from north, and inclination is the departure from the horizontal plane (shown with a dashed line). The small tick marks on the top left plot (N, E, S, W) mark the north, east, south, and west directions.

of the three PV tensors are nearly identical, so only one model is shown (Figure 11). We identified two distinct clusters of orientations that provided an acceptable fit to the data; for each orientation, the [100] and [010] axes are oblique from the horizontal, while the [001] axis is closer to horizontal (~20° away). Similarly, the Fp single-crystal elastic tensor also provided a fit to the observations (Figure 12, left column). All of the null observations align with directions for which weak splitting is predicted for this case. Because of the cubic symmetry of the Fp elastic tensor, there are multiple clusters on the orientation plots in Figure 12; however, we find that the two of the crystallographic axes for the best fitting Fp orientation are in the horizontal plane, with the other is in the vertical plane.

For the PPV texture models derived from the work of *Walker et al. [2011]*, we successfully identified orientations that fit the data for elastic tensors that invoke both (001) and (010) as the dominant slip planes; however, models that invoke (100) as the dominant slip plane did not successfully match the observations.

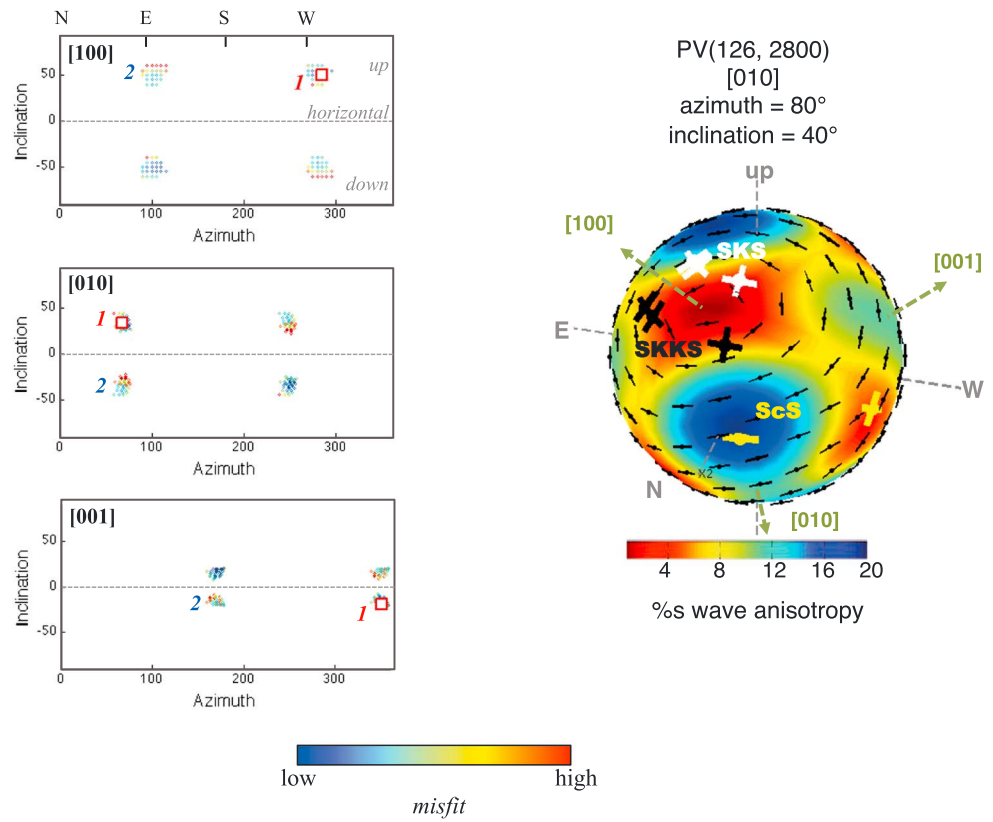


Figure 11. Plot of successful single-crystal PV fits for the New Zealand subregion. (right) A successful model fit for the PV elastic tensor of Wookey *et al.* [2005b], where the SKS (white), SKKS (black), and ScS (yellow) phases are plotted. The plotting conventions follow those of Figures 9 and 10. For this case, all of the null measurements are associated with ray propagation directions for which the elasticity model predicts weak anisotropy. (left) The best fitting orientations for PV in geographic space, following the plotting convention in Figure 10. The points plotted represent all of the acceptable fits to the elastic tensor; the orientation with the minimum misfit value is plotted with red squares. There are two clusters corresponding to distinct orientations that can fit the observed data (labeled 1 and 2, ranked based on minimum misfit of each cluster). Note that the observations from the southwestern Australia subregion could not be fit with the single-crystal PV tensor.

Examples of successful models using the textured PPV elastic tensors are shown in Figure 13. For the elastic tensors based on slip on the (010) plane, the successful scenarios usually attribute all of the null measurements to a propagation path associated with weak or absent splitting, while the (001) models attribute the ScS null measurements to an alignment of the initial polarization with the fast or slow direction and the SKS and SKKS nulls aligned with weak anisotropy. Figure 14 shows the distribution of the inferred shear planes and directions in geographic space for the successful PPV LPO models. For the elasticity model that invokes dominant slip on the (010) plane, the best fit orientation invokes a nearly vertical shear plane (that is, with a nearly horizontal shear plane normal) and a shear direction that is ~40° from the horizontal. For dominant slip on the (001) plane, we infer a likely nearly horizontal shear direction, with an azimuth of about N100°E, and an obliquely inclined shear plane.

3.2.2. Southwest Australia Subregion

The subregion beneath southwest Australia (Figure 8) encompasses four distinct raypaths (two for ScS, one for SKS, and one for SKKS); of these, three paths exhibit splitting and one is null. We tested an identical suite of forward models for this subregion as with New Zealand. We found that three of the four single-crystal PPV elastic tensors provided acceptable fits to the data, along with the MgO LPO elastic tensor and one of the three PPV LPO scenarios (that associated with dominant slip on the (010) plane). In contrast, no single-crystal PV or Fp elastic scenario fit the observations, and the SPO scenarios we tested were also found to be incompatible with the data. More details for each model are in Table 3.

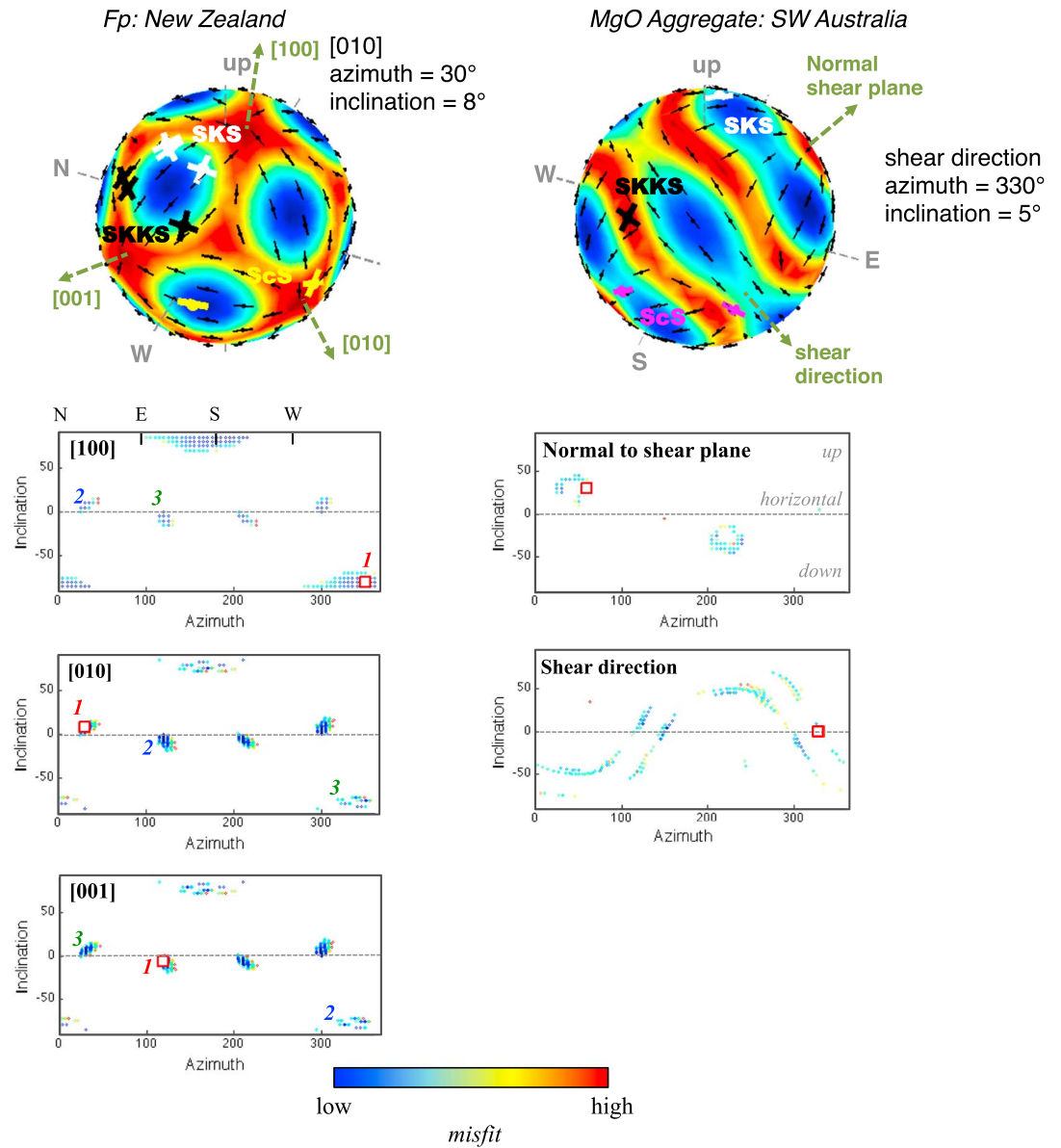


Figure 12. Plot of successful MgO aggregate [Long *et al.*, 2006] fits for southwestern Australia and single-crystal Fp [Karki *et al.*, 1999] fits for New Zealand. (top row) Successful model fits for each elastic tensor, with the SKS (white), SKKS (black), and ScS (yellow or magenta) phases plotted. (bottom row) All orientations that fit the observations. The plotting conventions follow Figures 9 and 10. The minimum misfit values are identified with a red square. For Fp, there are three clusters of distinct orientations, ranked by minimum misfit (1 = lowest misfit, 4 = largest misfit). For MgO aggregate, a number of orientations are possible for shear direction and cannot be constrained to a single cluster. However, the normal to the shear plane appears to show an obliquely inclined shear plane.

For single-crystal PPV, the data can be fit by splitting predictions for elastic constants calculated at conditions of 125 GPa and 2500 K from Wentzcovitch *et al.* [2006], as well as those calculated at conditions of 136 GPa/3000 K and 135 GPa/4000 K by Stackhouse *et al.* [2005]. An example of a good fit is shown in Figure 9 (right column). For each of the successful model cases, the null SKKS measurement was found to correspond to a direction for which weak or absent splitting was predicted. Our determination of best fit orientations (Figure 10) is defined by four distinct clusters of possible solutions, indicating that multiple orientations are consistent with the data and the anisotropy orientation is not well constrained by the observation. We have ranked the four possible orientations in Figure 10 based on the minimum misfit values in each cluster and find that Cluster #3 for southwest Australia has an orientation nearly identical to our best

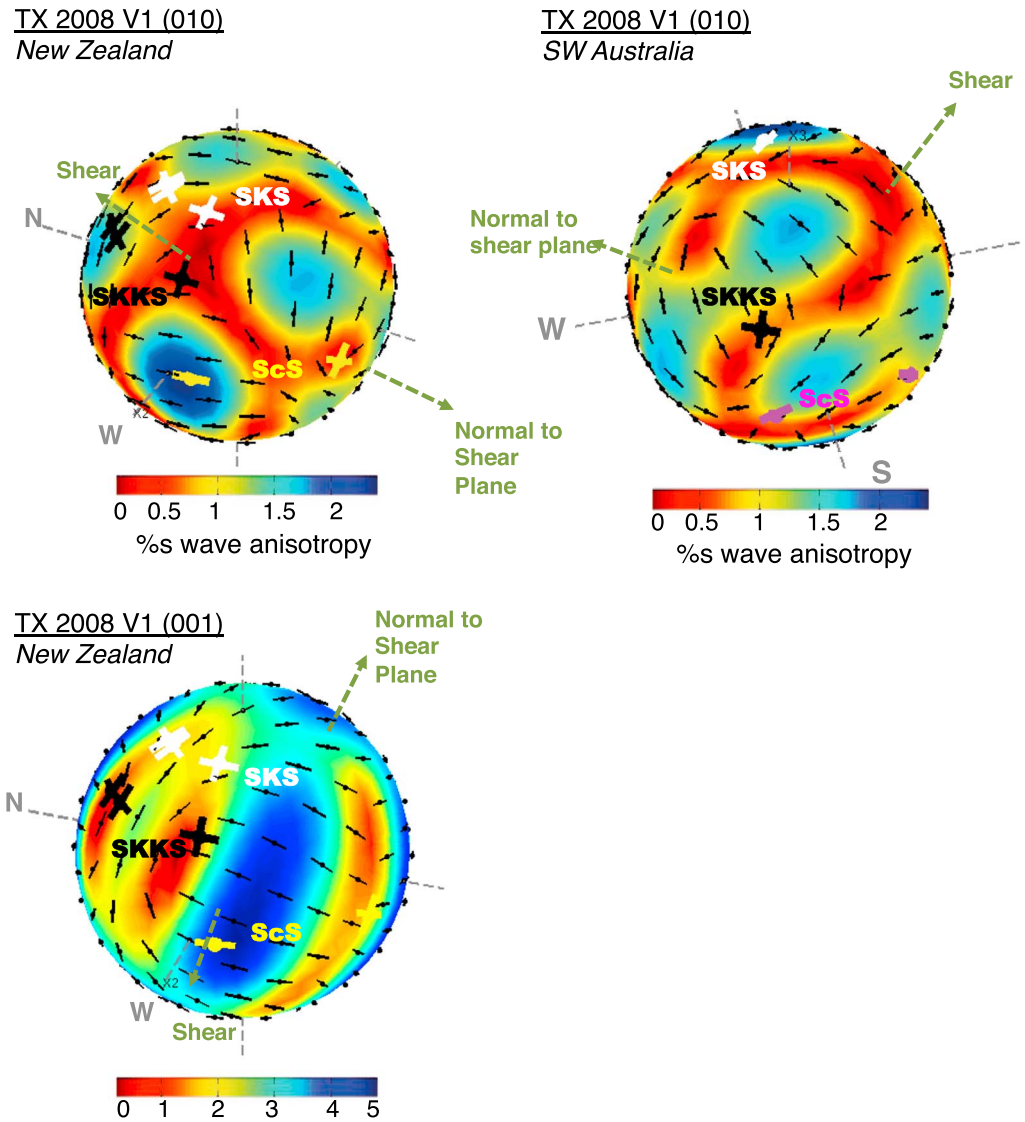


Figure 13. Examples of successful models using textured elastic tensors derived from the global flow models of Walker *et al.* [2011]. Plotting conventions are as in Figure 9. Each panel is labeled with the name of the subregion under consideration, as well as the model used to generate the elastic constants and the dominant slip plane, as described in the text. Each cluster of observations is colored based on the seismic phase (SKS, white; SKKS, black; ScS, magenta, or yellow). The shear direction and normal to the horizontal shear plane are labeled and are referred to in Figure 14.

fitting single-crystal PPV orientation for New Zealand, where they are ranked based on minimum misfit values in each cluster.

In contrast to our findings for the New Zealand subregion, we were able to identify plausible orientations for our MgO LPO elasticity tensor that are consistent with the observations (Figure 12, right column). The successful scenarios encompassed both possible explanations for the null SKKS measurement (weak splitting along that orientation or alignment of the back azimuth with the fast or slow axis). This elasticity scenario exhibits a complicated set of plausible geometries (Figure 12), with a range of geometries for the shear direction allowed by the data and with a likely shear plane normal that is oblique to the horizontal.

For the PPV LPO models from Walker *et al.* [2011], the results of the forward modeling (Figures 13 and 14) are somewhat similar to our findings for the New Zealand subregion. We identified acceptable models for elastic tensors that invoke dominant slip only on the (010) plane. The range of successful models attributes the SKKS null measurement either to weak splitting or an alignment of the back azimuth with the fast/slow direction.

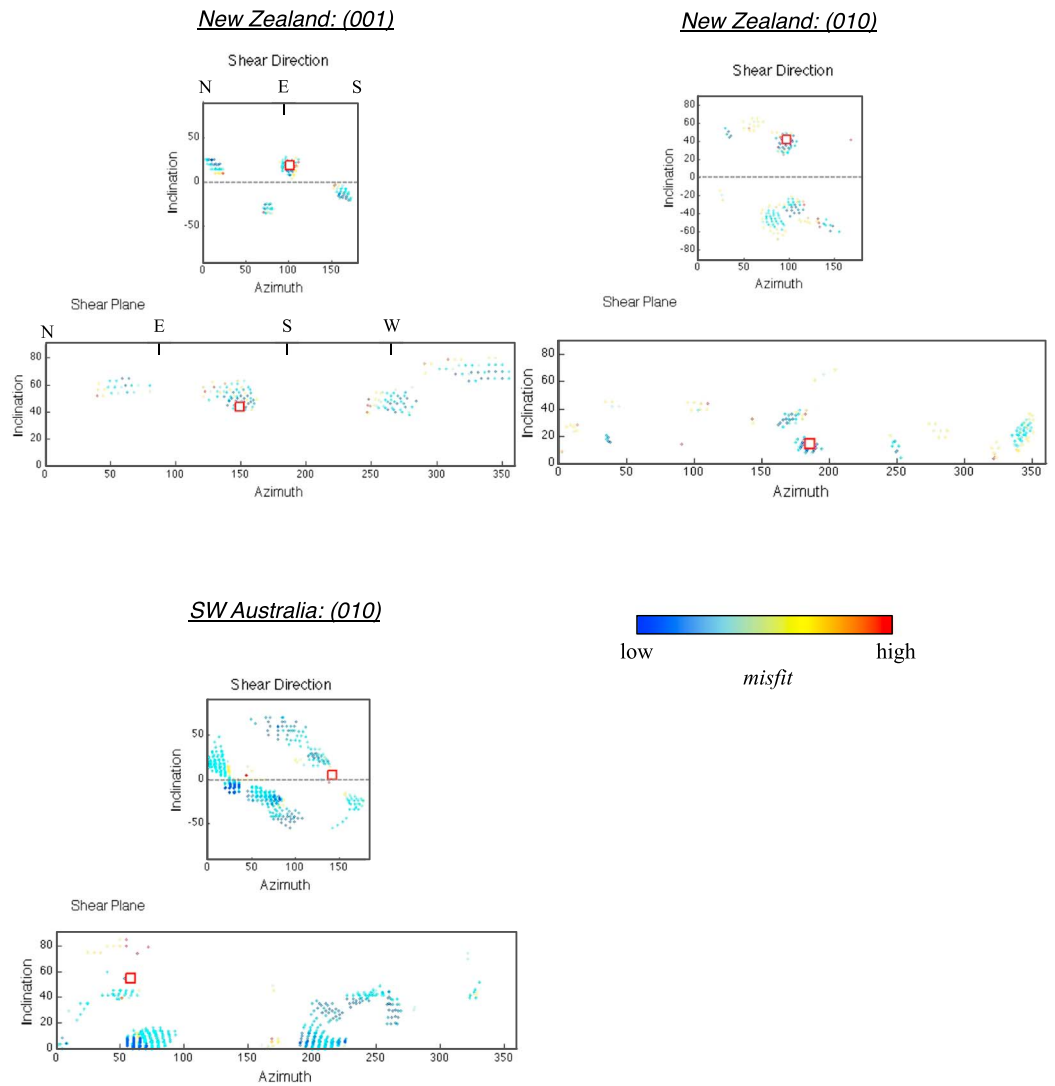


Figure 14. Plots of all scenarios with an acceptable fit to the data for the global flow model derived fabric of PPV. Shear direction indicates the direction of maximum shear, with its azimuth in the clockwise direction from north (N) and its inclination the angle from the horizontal plane. The shear plane geometry is represented by the vector normal to the shear plane. The plots are organized by dominant slip system and region. Each point is also colored by the smallest misfit value for that particular model. The white boxes indicate the orientations with the smallest misfit values.

The best fitting orientation for the elastic tensor that invokes slip on the (010) plane invokes a shear direction that is nearly horizontal (Figure 14), with an azimuth of approximately N140°E, and a shear plane normal inclined obliquely from the horizontal. We emphasize, however, that there is a large range of orientations that provide an acceptable fit to the observations for the (010) dominant slip plane beneath southwest Australia, so the best fitting orientation is by no means unique.

4. Discussion

The set of ScS, SKS, and SKKS splitting measurements presented in section 2 demonstrate that there is significant seismic anisotropy in the lowermost mantle beneath Australia, although the considerable variability in the data set argues for complexity in that structure. Taken together, our splitting measurements argue against a simple, pervasive transverse isotropy (that is, anisotropy with a hexagonal geometry) with either a vertical or a horizontal axis of symmetry (VTI or HTI). Instead, they indicate an anisotropic geometry that is more complicated than a VTI/HTI model and/or significant lateral variations in anisotropic structure throughout the study region. The SKS-SKKS data set mainly samples the region of the lowermost mantle

outside of the African and Pacific LLSVPs (Figure 5). The few *SKS-SKKS* pairs in our data set that sample the interior of the Pacific LLSVP do not show a contribution from D'' anisotropy. This is consistent with previous findings for the African LLSVP [Lynner and Long, 2014a], whose interior does not appear to exhibit strong anisotropy in a geometry that contributes to *SK(K)S* splitting. We do not, however, observe a clear pattern of *SKS-SKKS* splitting discrepancies near the LLSVP boundaries, as has been observed for the African LLSVP and the Perm Anomaly [Lynner and Long, 2014a; Long and Lynner, 2015]; instead, there are some discrepant *SKS-SKKS* pairs throughout the study region. We also see significant splitting of *ScS* paths that sample a region within the Pacific LLSVP beneath Papua New Guinea (Figure 6). Interestingly, this group of raypaths exhibits a transition in measured fast directions, from mostly NW-SE fast directions for paths that sample furthest into the LLSVP interior to NE-SW fast directions for paths that sample near the LLSVP border, even though the rays are propagating along similar azimuths. This may suggest a transition in anisotropic geometry near the LLSVP border, as has been proposed for the African LLSVP [Cottaar and Romanowicz, 2013].

Our forward modeling results, described in section 3, have allowed us to dramatically narrow the possible set of plausible anisotropic geometries that are compatible with two subgroups of our observations. One important implication of these tests is that we can generally rule out entire classes of possible anisotropy scenarios, including the melt SPO elasticity tensors we tested (except for the oblate SPO model for New Zealand), single-crystal PV (for New Zealand), single-crystal Fp (for New Zealand), or MgO LPO (for southwestern Australia). A consistent finding is that for the single-crystal PPV elastic tensors we could identify orientations that were consistent with the observations for both regions; similarly, for the PPV LPO tensors derived from texture modeling for horizontal simple shear at the base of the mantle, we were able to reliably identify permissible orientations for those tensors that invoked slip on the (001) (only for New Zealand) or (010) plane (both regions).

Of the 14 different elastic tensors considered in this study, the ones that were most reliably able to fit the observations in both subregions were associated with either single-crystal or textured PPV. Given this, and given that previous observational studies of D'' anisotropy have also identified PPV as a plausible scenario [e.g., Nowacki et al., 2010; Walker et al., 2011; Ford et al., 2015; Ford and Long, 2015], we focus our interpretation of our forward modeling results in terms of possible deformation geometries on PPV as the most likely cause of anisotropy. Furthermore, given that our study region is located outside of the two LLSVPs and we are thus sampling lowermost mantle material with average-to-fast isotropic *S* wave velocities, it is plausible that PPV, and not PV, is the stable magnesium silicate phase [Murakami et al., 2004]. We emphasize, however, that the other mechanisms (PV or Fp) discussed in section 3.2 are consistent with the data and should also be considered as possible, if less likely.

Based on our observations and forward modeling results, we can learn about likely deformation and flow geometries at the base of the mantle, using insights from the modeling to narrow the possibilities. Some assumptions are necessary, however, the most restrictive of which is that each subset of rays is sampling the same laterally homogenous anisotropic region. If small-scale heterogeneity in the anisotropic structure were present, that would be incompatible with this assumption; we generally observe, however, that there are multiple and consistent observations over the same region and azimuth. We further assume ray theoretical behavior and do not account for finite frequency effects. For the interpretation of our single-crystal elasticity results, we assume that the geometry (though not the strength) of splitting for a textured aggregate will be similar to that predicted for a single crystal, an assumption that is likely to be imperfect. For this case, we assume that the orientation of the single crystal aligns with the macroscopic strain geometry (for example, slip in the [100] direction would result in a [100] axis of PPV aligned with the shear direction). Alternatively, for the interpretation of our results using a modeled PPV texture, we do not need to make the assumption that the predicted splitting for the aggregate will resemble that of a single crystal; however, we do rely on the large number of assumptions that go into the texture modeling code (for example, relative strength of the different slip systems [Walker et al., 2011]). We further assume that deformation is being accommodated in the lowermost mantle via a dislocation creep mechanism, which is required to form LPO [Karato, 2012]. It has been suggested that dislocation creep might dominate in regions of the lower mantle near a downgoing slab impinging on the CMB, because the temperatures may be relatively low and the stresses relatively high, which favor dislocation creep [McNamara et al., 2001].

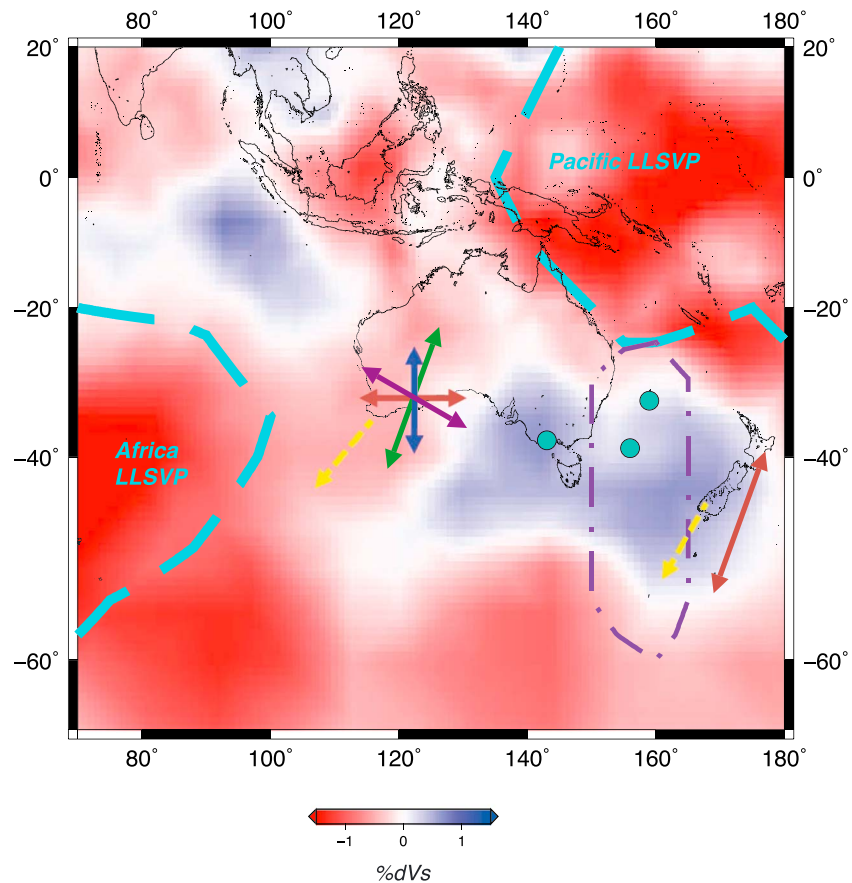


Figure 15. Interpretive map of possible orientations for the single-crystal results of PPV. Beneath New Zealand, only one orientation of PPV (red arrow) fit the observed data, where the best fit solution for the [100] direction is plotted. Beneath southwestern Australia, we plot each horizontal component of the [100] direction of each cluster from Figure 10, with arrow colors corresponding to the cluster groups. The length of the arrows illustrates how large the horizontal projection of the axis is (that is, shorter arrows are closer to vertical, while longer arrows are closer to horizontal). For cluster 3 (green arrow), the [100] axis is nearly horizontal while cluster 1 (red arrow) is inclined $\sim 45^\circ$. The yellow dashed arrows show the predicted horizontal mantle flow direction for particular region from the TX2008.V1 global mantle flow model [Simmons *et al.*, 2009; Walker *et al.*, 2011].

There is a great deal of uncertainty still in the literature about the dominant deformation mechanisms for lowermost mantle minerals, including Fp [e.g., Karato, 1998; Yamazaki and Karato, 2002; Long *et al.*, 2006; Carrez and Cordier, 2009], PV [e.g., Merkel *et al.*, 2003; Cordier *et al.*, 2004; Mainprice *et al.*, 2008], and PPV [e.g., Merkel *et al.*, 2007; Miyagi *et al.*, 2010; Nowacki *et al.*, 2011; Goryaeva *et al.*, 2016]. This uncertainty is due in large part to the difficulty of doing deformation experiments at the relevant pressure and temperature conditions; many of the available experimental data were obtained at room temperature, at pressures lower than those of the lower mantle, and/or on analog materials.

Beneath New Zealand, our modeling for single-crystal PPV (Figure 10) suggests that the [100] axis is near horizontal (slightly oblique), with an azimuth of roughly $N15^\circ E$, and the [001] and [010] axes are oblique ($\sim 45^\circ$). The macroscopic shear direction inferred for this geometry would depend on the dominant slip system, since shear in the mantle is likely generally parallel to the dominant slip direction [Karato, 2012]. There is debate around the dominant slip direction for PPV. Experimental and theoretical studies have variously suggested that the dominant slip direction could be [100] or [010], while the dominant slip plane could be the (110), (001), (100), or (010) planes, as summarized in Nowacki *et al.* [2011], Cottaar *et al.* [2014], and Goryaeva *et al.* [2016]. If the dominant slip system of PPV were more precisely known, then our modeling results would more tightly constrain possible deformation geometry in these locations. For example, if [010] is the dominant slip direction, as suggested by Miyagi *et al.* [2010], we would infer a mantle shear

direction that is highly oblique to the horizontal (inclined $\sim 50^\circ$ downward) with an azimuth of about N270°E for the New Zealand subregion (Figure 10). If, instead, the [100] direction represents the dominant slip direction [Yamazaki *et al.*, 2006], we would infer a nearly horizontal shear direction, suggesting generally horizontal flow, with a direction roughly NNE-SSW (red arrow beneath New Zealand in Figure 15). This possible scenario, which invokes the [100] axis as the dominant slip direction, would be generally consistent with the prediction that subducting slabs may drive horizontal flow at the base of the mantle [e.g., McNamara *et al.*, 2002].

In context of our model results based on textured PPV aggregates derived from the global models of Walker *et al.* [2011], an oblique shear direction and shear plane normal seem the most likely deformation geometry beneath New Zealand (Figure 14), regardless of whether the dominant slip plane is (010) or (001). The best fit orientations for New Zealand are complicated and do not resemble simple shear with a horizontal shear plane, but rather an inclined shear plane with an inclined shear direction. The most likely explanations for this complicated deformation geometry invokes a combination of lateral and vertical gradients in flow velocity or perhaps a component of pure shear in addition to simple shear.

Beneath southwestern Australia, our single-crystal modeling results for PPV suggest a range of possible orientations, with the [100] axis varying from oblique to horizontal, all possible [010] directions oriented oblique to the horizontal plane, and the [001] axis varying from oblique to horizontal (Figure 10). The third of the possible four orientations (Cluster 3 as defined in Figure 10) is consistent with the best fit orientation for single-crystal PPV for New Zealand, which could indicate that the orientation of PPV is similar for both regions. If true, this inference would be consistent with the prediction from the Walker *et al.* [2011] flow model that the lowermost mantle flow direction should be similar beneath both of our subregions (dashed yellow arrows in Figure 15). For this cluster 3 orientation, the [100] direction would suggest a nearly north-south horizontal macroscopic shear direction. A [010] dominant slip direction would imply a shear direction aligned nearly east-west (Figure 15). However, this inference on possible flow directions is not unique, as there are three other possible orientations that are consistent with the splitting observations (Figure 10).

In context of our model results for southwest Australia based on textured PPV aggregates, horizontal shear would be the likeliest deformation geometry based on the minimum misfit orientation, but the shear direction inclination can vary quite significantly and still fit the observations (Figure 14). The scatter in possible models in Figure 14 shows that a range of possible deformation geometries are plausible, including those that invoke a nearly vertical shear direction.

We can compare the plausible horizontal flow directions found in this study to global mantle flow models [Simmons *et al.*, 2009; Walker *et al.*, 2011]. We find that there is at least some agreement between the lowermost mantle flow directions predicted beneath our subregions in the global flow models (model TX2008.V1 from Walker *et al.* [2011]) and those flow directions inferred from our modeling (Figure 15), if we assume that [100] is the dominant slip direction in PPV, as we have in our previous work [Ford *et al.*, 2015]. For southwestern Australia, the global flow models predict generally horizontal flow directed to the southwest (yellow arrows in Figure 15). While there are multiple possible orientations of the [100] axis based on single-crystal PPV tensors, cluster 3 is within $\sim 10^\circ$ of the mantle flow direction predicted by Walker *et al.* [2011]. Beneath New Zealand, global flow models predict a similar mantle flow direction as beneath southwestern Australia, with flow to the southwest, but with a downwelling component likely due to a high-density anomaly in the lower mantle (yellow arrows in Figure 15) [Simmons *et al.*, 2009]. For comparison, the geodynamic mantle flow models in Walker *et al.* [2011] predict relatively simple horizontal flow at the base of the mantle beneath Australia. This predicted flow direction appears to be nearly identical to our modeling results from the single-crystal elastic tensor of PPV, if [100] is the dominant slip direction (Figure 15). Other assumptions about the dominant slip systems in PPV, however, yield different inferences on flow direction, which are not consistent with the global flow model predictions, including slip in the [010] direction (for single-crystal PPV) and slip on the (010) and (001) planes (for the textured aggregates). To summarize, there appears to be some agreement between the global flow models of Walker *et al.* [2011] and our anisotropy observations assuming slip in the [100] direction; however, a more detailed analysis comparing the predictions from a suite of different global flow models is an important next step.

It is instructive to compare our results to those of Ford *et al.* [2015], who applied the same forward modeling technique to a data set that samples the lowermost mantle beneath the Afar region of Africa. Similar to that study, which focused on single-crystal elastic tensors, our results suggest that PPV represents the most likely cause for lowermost mantle anisotropy. In the Ford *et al.* [2015] study, the preferred geometry for single-crystal PPV invokes a nearly vertical or oblique [100] axis and nearly horizontal directions for the other axes. This contrasts with our findings in this study, which for the region beneath New Zealand (the better constrained of our two subregions) invokes a nearly horizontal [100] axis. We note that the regions under study are very different; the Ford *et al.* [2015] study focuses on the edge of an LLSVP and invokes either plume-related upwelling or the vertical deflection of flow, while this study focuses on a region located outside of the LLSVPs. Both the present study and Ford *et al.* [2015] found that for the model fits using the textured PPV elastic constants derived from the study of Walker *et al.* [2011], those elasticity models with dominant slip on the (010) and/or (001) planes provided the best fits to the data.

5. Summary

We have presented a data set of 103 pairs of SKS-SKKS splitting measurements and 72 S-ScS splitting measurements that constrain seismic anisotropy in the lowermost mantle beneath Australia. The data set exhibits considerable complexity, suggesting a departure from the simplest anisotropy scenarios (such as widespread VTI or HTI anisotropy) and likely heterogeneity in anisotropic structure. Within our study region, we have identified two much smaller subregions for which we have observations over a range of ray propagation directions and have implemented a forward modeling framework that assumes a uniform anisotropy within each subregion. We tested a suite of elastic tensor scenarios and found that we were able to rule out several scenarios as incompatible with the observations; for other scenarios, our modeling was able to constrain what orientation(s) of the elastic tensor provided a satisfactory fit to the data.

For the New Zealand subregion, single-crystal PV, Fp, or PPV appear to provide good fits to the observed data. Based on the single-crystal results for PPV, horizontal flow is possible (if [100] is the dominant slip direction and is inferred to be nearly parallel to the macroscopic shear direction). Texture development calculations for PPV also fit the observations for cases in which the dominant slip plane is either (010) or (001). While there are several possible scenarios for mantle flow directions based on our LPO models of PPV, our preferred scenario invokes a complicated deformation geometry that is oblique to the horizontal plane at the base of the mantle beneath New Zealand. Beneath southwestern Australia, the LPO model of MgO and PPV both provide good fits to the observations, as does textured PPV. Based on the single-crystal results for PPV, horizontal flow is possible (assuming the orientation associated with cluster 3 in Figure 12 and a [100] dominant slip direction); however, other orientations are also possible. Our results based on textured PPV aggregates suggest that (010) is the likely dominant slip plane. We suggest that horizontal flow is a possible scenario in the lowermost mantle beneath southwestern Australia, based on our modeling results using elasticity for textured LPO aggregates, but other geometries are possible. Future improvements in our knowledge of the dominant slip systems in PPV and other lowermost mantle minerals [e.g., Goryaeva *et al.*, 2016] will enhance our ability to relate observations and models of D" anisotropy such as those presented in this study to deformation geometry.

Acknowledgments

This work was supported by a National Science Foundation (NSF) Graduate Research Fellowship grant DGE-1122492 to N.C. and by NSF grant EAR-1547499 to M.D.L. Some figures were prepared using the Generic Mapping Tools [Wessel and Smith, 1991]. We used data from the Global Seismographic Network, Geoscope, and the Global Telemetered Seismograph Network. All data were downloaded from the Data Management Center (DMC) of the Incorporated Research Institutions for Seismology (IRIS). We are grateful to Sébastien Merkel and an anonymous reviewer for constructive comments that helped to improve the paper.

References

- Austermann, J., B. T. Kaye, J. X. Mitrovica, and P. Huybers (2014), A statistical analysis of the correlation between large igneous provinces and lower mantle seismic structure, *Geophys. J. Int.*, *197*(1), 1–9, doi:10.1093/gji/ggt500.
- Burke, K., B. Steinberger, T. H. Torsvik, and M. A. Smethurst (2008), Plume generation zones at the margins of large low shear velocity provinces on the core–mantle boundary, *Earth Planet. Sci. Lett.*, *265*(1–2), 49–60, doi:10.1016/j.epsl.2007.09.042.
- Carrez, P., and P. Cordier (2009), Peierls-Nabarro modelling of dislocations in MgO from ambient pressure to 100 GPa, *Modell. Simul. Mater. Sci. Eng.*, *17*(3), 035010.
- Chaloner, J. W., C. Thomas, and A. Rietbrock (2009), P- and S-wave reflectors in D" beneath southeast Asia, *Geophys. J. Int.*, *179*(2), 1080–1092, doi:10.1111/j.1365-246X.2009.04328.x.
- Cordier, P., T. Ungár, L. Zsoldos, and G. Tichy (2004), Dislocation creep in MgSiO₃ perovskite at conditions of the Earth's uppermost lower mantle, *Nature*, *428*(6985), 837–840, doi:10.1038/nature02472.
- Cottaar, S., and B. Romanowicz (2013), Observations of changing anisotropy across the southern margin of the African LLSVP, *Geophys. J. Int.*, *195*(2), 1184–1195, doi:10.1093/gji/ggt285.
- Cottaar, S., M. Li, A. K. McNamara, B. Romanowicz, and H. R. Wenk (2014), Synthetic seismic anisotropy models within a slab impinging on the core–mantle boundary, *Geophys. J. Int.*, *199*(1), 164–177, doi:10.1093/gji/ggu244.

- Crotwell, H. P., T. J. Owens, and J. Ritsema (1999), The TauP toolkit: Flexible seismic travel-time and ray-path utilities, *Seismol. Res. Lett.*, *70*(2), 154–160, doi:10.1785/gssrl.70.2.154.
- Davaille, A. (1999), Simultaneous generation of hotspots and superswells by convection in a heterogeneous planetary mantle, *Nature*, *402*(6763), 756–760, doi:10.1038/45461.
- Davies, D. R., S. Goes, J. H. Davies, B. S. A. Schuberth, H. P. Bunge, and J. Ritsema (2012), Reconciling dynamic and seismic models of Earth's lower mantle: The dominant role of thermal heterogeneity, *Earth Planet. Sci. Lett.*, *353–354*, 253–269, doi:10.1016/j.epsl.2012.08.016.
- Dziewonski, A. M., and D. L. Anderson (1981), Preliminary reference Earth model, *Phys. Earth Planet. Inter.*, *25*(4), 297–356.
- Ford, H. A., and M. D. Long (2015), A regional test of global models for flow, rheology, and seismic anisotropy at the base of the mantle, *Phys. Earth Planet. Inter.*, *245*, 71–75, doi:10.1016/j.pepi.2015.05.004.
- Ford, H. A., M. D. Long, X. He, and C. Lynner (2015), Lowermost mantle flow at the eastern edge of the African Large Low Shear Velocity Province, *Earth Planet. Sci. Lett.*, *420*, 12–22, doi:10.1016/j.epsl.2015.03.029.
- French, S. W., and B. Romanowicz (2015), Broad plumes rooted at the base of the Earth's mantle beneath major hotspots, *Nature*, *525*(7567), 95–99, doi:10.1038/nature14876.
- Garnero, E. J., and A. K. McNamara (2008), Structure and dynamics of Earth's lower mantle, *Science*, *320*(5876), 626–628, doi:10.1126/science.1148028.
- Goryaeva, A. M., P. Carrez, and P. Cordier (2016), Low viscosity and high attenuation in MgSiO₃ post-perovskite inferred from atomic-scale calculations, *Sci. Rep.*, *6*, 34771, doi:10.1038/srep34771.
- Hernlund, J. W., and S. Labrosse (2007), Geophysically consistent values of the perovskite to post-perovskite transition Clapeyron slope, *Geophys. Res. Lett.*, *34*, L05309, doi:10.1029/2006GL028961.
- Hernlund, J. W., and A. K. McNamara (2015), 7.11 - The core-mantle boundary region, *Treatise Geophys.*, *2*(7), 461–519, doi:10.1016/B978-0-444-53802-4.00136-6.
- Karato, S. I. (1998), Some remarks on the origin of seismic anisotropy in the "D" layer, *Earth Planets Space*, *50*(11–12), 1019–1028, doi:10.1186/BF03352196.
- Karato, S. (2012), *Deformation of Earth Materials: An Introduction to the Rheology of Solid Earth*, pp. 255–270, Cambridge Univ. Press, New York.
- Karki, B. B., R. M. Wentzcovitch, S. Gironcoli, and S. Baroni (1999), First-principles determination of elastic anisotropy and wave velocities of MgO at lower mantle conditions, *Science*, *286*(5445), 1705–1707, doi:10.1126/science.286.5445.1705.
- Kendall, J.-M., and P. G. Silver (1998), Investigating causes of "D" anisotropy, in *The Core-Mantle Boundary Region*, edited by M. Gurnis et al., pp. 97–118, AGU, Washington, D. C.
- Kennett, B. L. N., E. R. Engdahl, and R. Buland (1995), Constraints on seismic velocities in the Earth from travel-times, *Geophys. J. Int.*, *122*(1), 108–124, doi:10.1111/j.1365-246X.1995.tb03540.x.
- Lay, T., and D. V. Helmberger (1983), The shear-wave velocity gradient at the base of the mantle, *J. Geophys. Res.*, *88*, 8160–8170, doi:10.1029/JB088iB10p08160.
- Lekic, V., S. Cottaar, A. Dziewonski, and B. Romanowicz (2012), Cluster analysis of global lower mantle tomography: A new class of structure and implications for chemical heterogeneity, *Earth Planet. Sci. Lett.*, *357–358*, 68–77, doi:10.1016/j.epsl.2012.09.014.
- Long, M. D. (2009), Complex anisotropy in D" beneath the eastern Pacific from SKS–SKKS splitting discrepancies, *Earth Planet. Sci. Lett.*, *283*(1–4), 181–189, doi:10.1016/j.epsl.2009.04.019.
- Long, M. D., and C. Lynner (2015), Seismic anisotropy in the lowermost mantle near the Perm Anomaly, *Geophys. Res. Lett.*, *42*(17), 7073–7080, doi:10.1002/2015GL065506.
- Long, M. D., X. Xiao, Z. Jiang, B. Evans, and S. Karato (2006), Lattice preferred orientation in deformed polycrystalline (Mg,Fe)O and implications for seismic anisotropy in D", *Phys. Earth Planet. Inter.*, *156*(1–2), 75–88, doi:10.1016/j.pepi.2006.02.006.
- Lynner, C., and M. D. Long (2013), Sub-slab seismic anisotropy and mantle flow beneath the Caribbean and Scotia subduction zones: Effects of slab morphology and kinematics, *Earth Planet. Sci. Lett.*, *361*, 367–378, doi:10.1016/j.epsl.2012.11.007.
- Lynner, C., and M. D. Long (2014a), Lowermost mantle anisotropy and deformation along the boundary of the African LLSVP, *Geophys. Res. Lett.*, *41*, 3438–3446, doi:10.1002/2014GL059875.
- Lynner, C., and M. D. Long (2014b), Sub-slab anisotropy beneath the Sumatra and circum-Pacific subduction zones from source-side shear wave splitting observations, *Geochem. Geophys. Geosyst.*, *15*, 2262–2281, doi:10.1002/2014GC005239.
- Mainprice, D., A. Tommasi, D. Ferré, P. Carrez, and P. Cordier (2008), Predicted glide systems and crystal preferred orientations of polycrystalline silicate Mg-perovskite at high pressure: Implications for the seismic anisotropy in the lower mantle, *Earth Planet. Sci. Lett.*, *271*(1), 135–144, doi:10.1016/j.epsl.2008.03.058.
- McNamara, A. K., and S. Zhong (2005), Thermochemical structures beneath Africa and the Pacific Ocean, *Nature*, *437*(7062), 1136–1139, doi:10.1038/nature04066.
- McNamara, A. K., S. I. Karato, and P. E. van Keken (2001), Localization of dislocation creep in the lower mantle: Implications for the origin of seismic anisotropy, *Earth Planet. Sci. Lett.*, *191*(1–2), 85–99, doi:10.1016/S0012-821X(01)00405-8.
- McNamara, A. K., P. E. van Keken, and S. I. Karato (2002), Development of anisotropic structure in the Earth's lower mantle by solid-state convection, *Nature*, *416*(6878), 310–314, doi:10.1038/416310a.
- Meade, C., P. G. Silver, and S. Kaneshima (1995), Laboratory and seismological observations of lower mantle isotropy, *Geophys. Res. Lett.*, *22*, 1293–1296, doi:10.1029/95GL01091.
- Merkel, S., H. R. Wenk, J. Badro, G. Montagnac, P. Gillet, H. K. Mao, and R. J. Hemley (2003), Deformation of (Mg 0.9, Fe 0.1) SiO₃ perovskite aggregates up to 32 GPa, *Earth Planet. Sci. Lett.*, *209*(3), 351–360, doi:10.1016/S0012-821X(03)00098-0.
- Merkel, S., A. K. McNamara, A. Kubo, S. Speziale, L. Miyagi, Y. Meng, T. S. Duffy, and H. R. Wenk (2007), Deformation of (Mg, Fe) SiO₃ post-perovskite and "D" anisotropy, *Science*, *316*(5832), 1729–1732, doi:10.1126/science.1140609.
- Miyagi, L., W. Kanitpanyacharoen, P. Kaercher, K. K. Lee, and H. R. Wenk (2010), Slip systems in MgSiO₃ post-perovskite: Implications for D' anisotropy, *Science*, *329*(5999), 1639–1641, doi:10.1126/science.1192465.
- Mohiuddin, A., M. D. Long, and C. Lynner (2015), Mid-mantle seismic anisotropy beneath southwestern Pacific subduction systems and implications for mid-mantle deformation, *Phys. Earth Planet. Inter.*, *245*, 1–14, doi:10.1016/j.pepi.2015.05.003.
- Murakami, M., K. Hirose, K. Kawamura, N. Sata, and Y. Ohishi (2004), Post-perovskite phase transition in MgSiO₃, *Science*, *304*(5672), 855–858, doi:10.1126/science.1095932.
- Ni, S., E. Tan, M. Gurnis, and D. Helmberger (2002), Sharp sides to the African superplume, *Science*, *296*(5574), 1850–1852, doi:10.1126/science.1070698.
- Niu, F., and A. M. Perez (2004), Seismic anisotropy in the lower mantle: A comparison of waveform splitting of SKS and SKKS, *Geophys. Res. Lett.*, *31*, L24612, doi:10.1029/2004GL021196.

- Nowacki, A., and J. Wookey (2016), The limits of ray theory when measuring shear wave splitting in the lowermost mantle with ScS waves, *Geophys. J. Int.*, *207*(3), 1573–1583, doi:10.1093/gji/ggw358.
- Nowacki, A., J. Wookey, and J. M. Kendall (2010), Deformation of the lowermost mantle from seismic anisotropy, *Nature*, *467*, 1091–1094, doi:10.1038/nature09507.
- Nowacki, A., J. Wookey, and J. M. Kendall (2011), New advances in using seismic anisotropy, mineral physics and geodynamics to understand deformation in the lowermost mantle, *J. Geodyn.*, *52*(3–4), 205–228, doi:10.1016/j.jog.2011.04.003.
- Savage, M. K. (1999), Seismic anisotropy and mantle deformation: What have we learned from shear wave splitting?, *Rev. Geophys.*, *37*, 65–106, doi:10.1029/98RG02075.
- Shen, X., Y. Zhou, K. Idehara, X. Mei, and K. Xu (2014), An examination of the presence and topography of the D" discontinuity under the Russia–Kazakhstan border region using seismic waveform data from a deep earthquake in Spain, *Earthquake Sci.*, *2*(27), 209–215, doi:10.1007/s11589-014-0071-2.
- Silver, P. G., and W. W. Chan (1991), Shear wave splitting and subcontinental mantle deformation, *J. Geophys. Res.*, *96*, 16,429–16,454, doi:10.1029/91JB00899.
- Silver, P. G., and M. K. Savage (1994), The interpretation of shear-wave splitting parameters in the presence of two anisotropic layers, *Geophys. J. Int.*, *119*(3), 949–963, doi:10.1111/j.1365-246X.1994.tb04027.x.
- Silver, P. G., and M. D. Long (2011), The non-commutivity of shear wave splitting operators at low frequencies and implications for anisotropy tomography, *Geophys. J. Int.*, *184*(3), 1415–1427, doi:10.1111/j.1365-246X.2010.04927.x.
- Simmons, N. A., A. M. Forte, and S. P. Grand (2009), Joint seismic, geodynamic and mineral physical constraints on three-dimensional mantle heterogeneity: Implications for the relative importance of thermal versus compositional heterogeneity, *Geophys. J. Int.*, *177*(3), 1284–1304, doi:10.1111/j.1365-246X.2009.04133.x.
- Simmons, N. A., A. M. Forte, L. Boschi, and S. P. Grand (2010), GyPSuM: A joint tomographic model of mantle density and seismic wave speeds, *J. Geophys. Res.*, *115*, B12310, doi:10.1029/2010JB007631.
- Stackhouse, S., and J. P. Brodholt (2007), The high-temperature elasticity of MgSiO₃ post-perovskite. in *Post-Perovskite: The Last Mantle Phase Transition*, edited by K. Hirose, pp. 99–113, AGU, Washington, D. C., doi:10.1029/174GM09.
- Stackhouse, S., J. P. Brodholt, J. Wookey, J. M. Kendall, and G. D. Price (2005), The effect of temperature on the seismic anisotropy of the perovskite and post-perovskite polymorphs of MgSiO₃, *Earth Planet. Sci. Lett.*, *230*(1–2), 1–10, doi:10.1016/j.epsl.2004.11.021.
- Stadler, G., M. Gurnis, C. Burstedde, L. C. Wilcox, L. Alisic, and O. Ghattas (2010), The dynamics of plate tectonics and mantle flow: From local to global scales, *Science*, *329*(5995), 1033–1038, doi:10.1126/science.1191223.
- Steinberger, B. (2000a), Plumes in a convecting mantle: Models and observations for individual hotspots, *J. Geophys. Res.*, *105*, 11,127–11,152, doi:10.1029/1999JB900398.
- Steinberger, B. (2000b), Slabs in the lower mantle—Results of dynamic modelling compared with tomographic images and the geoid, *Phys. Earth Planet. Inter.*, *118*(3–4), 241–257, doi:10.1016/S0031-9201(99)00172-7.
- Sun, D., D. Helmberger, M. S. Miller, and J. M. Jackson (2016), Major disruption of D" beneath Alaska, *J. Geophys. Res. Solid Earth*, *121*, 3534–3556, doi:10.1002/2015JB012534.
- Thomas, C., J. M. Kendall, and J. Lowman (2004), Lower-mantle seismic discontinuities and the thermal morphology of subducted slabs, *Earth Planet. Sci. Lett.*, *225*(1–2), 105–113, doi:10.1016/j.epsl.2004.05.038.
- Torsvik, T. H., M. A. Smethurst, K. Burke, and B. Steinberger (2006), Large igneous provinces generated from the margins of the large low-velocity provinces in the deep mantle, *Geophys. J. Int.*, *167*(3), 1447–1460, doi:10.1111/j.1365-246X.2006.03158.x.
- Usui, Y., Y. Hiramoto, M. Furumoto, and M. Kanao (2005), Thick and anisotropic D" layer beneath Antarctic Ocean, *Geophys. Res. Lett.*, *32*, L13311, doi:10.1029/2005GL022622.
- Vidale, J. E. (1986), Complex polarization analysis of particle motion, *Bull. Seismol. Soc. Am.*, *76*(5), 1393–1405.
- Walker, A. M., and J. Wookey (2012), MSAT—A new toolkit for the analysis of elastic and seismic anisotropy, *Comput. Geosci.*, *49*, 81–90, doi:10.1016/j.cageo.2012.05.031.
- Walker, A. M., A. M. Forte, J. Wookey, A. Nowacki, and J. M. Kendall (2011), Elastic anisotropy of D" predicted from global models of mantle flow, *Geochem. Geophys. Geosyst.*, *12*, Q10006, doi:10.1029/2011GC003732.
- Wang, Y., and L. Wen (2007), Geometry and P and S velocity structure of the "African anomaly", *J. Geophys. Res.*, *112*, B05313, doi:10.1029/2006JB004483.
- Wentzcovitch, R. M., T. Tsuchiya, and J. Tsuchiya (2006), MgSiO₃ postperovskite at D" conditions, *Proc. Natl. Acad. Sci. U.S.A.*, *103*(3), 543–546, doi:10.1073/pnas.0506879103.
- Wessel, P., and W. H. Smith (1991), Free software helps map and display data, *Eos Trans. AGU*, *72*(41), 441–446.
- Whittaker, S., M. S. Thorne, N. C. Schmerr, and L. Miyagi (2015), Seismic array constraints on the D" discontinuity beneath Central America, *J. Geophys. Res. Solid Earth*, *121*, 1–18, doi:10.1002/2015JB012392.
- Wookey, J., and J. M. Kendall (2008), Constraints on lowermost mantle mineralogy and fabric beneath Siberia from seismic anisotropy, *Earth Planet. Sci. Lett.*, *275*(1–2), 32–42, doi:10.1016/j.epsl.2008.07.049.
- Wookey, J., J. M. Kendall, and G. Rüpker (2005a), Lowermost mantle anisotropy beneath the north Pacific from differential S-ScS splitting, *Geophys. J. Int.*, *161*(3), 829–838, doi:10.1111/j.1365-246X.2005.02623.x.
- Wookey, J., S. Stackhouse, J. M. Kendall, J. Brodholt, and G. D. Price (2005b), Efficacy of the post-perovskite phase as an explanation for lowermost-mantle seismic properties, *Nature*, *438*(7070), 1004–1007, doi:10.1038/nature04345.
- Wüstefeld, A., G. Bokelmann, C. Zanolli, and G. Barruol (2008), SplitLab: A shear-wave splitting environment in Matlab, *Comput. Geosci.*, *34*(5), 515–528, doi:10.1016/j.cageo.2007.08.002.
- Yamazaki, D., and S. I. Karato (2002), Fabric development in (Mg,Fe)O during large strain, shear deformation: Implications for seismic anisotropy in Earth's lower mantle, *Phys. Earth Planet. Inter.*, *131*(3), 251–267, doi:10.1016/S0031-9201(02)00037-7.
- Yamazaki, D., T. Yoshino, H. Ohfuji, J. I. Ando, and A. Yoneda (2006), Origin of seismic anisotropy in the D" layer inferred from shear deformation experiments on post-perovskite phase, *Earth Planet. Sci. Lett.*, *252*(3), 372–378, doi:10.1016/j.epsl.2006.10.004.
- Young, C. J., and T. Lay (1987), Evidence for a shear velocity discontinuity in the lower mantle beneath India and the Indian Ocean, *Phys. Earth Planet. Inter.*, *49*(1–2), 37–53, doi:10.1016/0031-9201(87)90131-2.